Microdissected tumor cuboids: a microscale cancer model for large-scale testing that retains a complex tumor microenvironment

Lisa F Horowitz[1*], Ricard Rodriguez-Mias[2], Marina Chan[3], Songli Zhu[3], Noah R Gottshall[1], Ivan Stepanov[1,4], Casey Stiles[1,5], Marcus Yeung[3], Tran NH Nguyen[1,6], Ethan J Lockhart[1], Raymond S Yeung[7], Judit Villen[2], Taranjit S Gujral[3], and Albert Folch[1]

Affiliations

[1] Department of Bioengineering, University of Washington, Seattle, WA, USA.
[2] Department of Genome Sciences, University of Washington, Seattle, WA, USA.
[3] Human Biology Division, Fred Hutchinson Cancer Research Center, Seattle, WA, USA.
[4] Department of Mechanical Engineering, University of Washington, Seattle, WA, USA.
[5] Department of Chemical Engineering, University of Washington, Seattle, WA, USA.
[6] Department of Biochemistry, University of Washington, Seattle, WA, USA.
[7] Department of Surgery, University of Washington, Seattle, WA, USA.
[*] Corresponding author. Email: lhorowit@gmail.com

Abstract

To bridge the gap between bench and bedside, there is a need for more faithful models of human cancers that can recapitulate key features of the human tumor microenvironment (TME) and simultaneously facilitate large-scale drug tests. Our recently developed microdissection method optimizes the yield of large numbers of cuboidal microtissues ("cuboids", ~(400 µm)^3) from a tumor biopsy. Here we demonstrate that cuboids from syngeneic mouse tumor models and human tumors retain a complex TME, making them amenable for drug and immunotherapy evaluation. We characterize relevant TME parameters, such as cellular architecture, cytokine secretion, proteomics profiles, and response to drug panels in multi-well arrays. Despite the cutting procedure and the time spent in culture (up to 7 days), the cuboids display strong cytokine expression and drug responses, including to immunotherapy. Overall, our results suggest that cuboids could provide essential therapeutic information for personalized oncology applications and could help the development of TME-dependent therapeutics and cancer disease models, including for clinical trials.

Introduction

One of the main challenges in oncology is that every solid tumor and the environment it grows in are unique, determining therapeutic outcomes. Targeted therapies and immunotherapies have seen spectacular successes in some patients, but the reality is that most patients do not benefit from these approaches, even when guided by genetics.[1] For this reason, for almost a century researchers have utilized functional tests, generally based on tissue cultures and patient-derived xenografts (PDXs), that address the limited amount of human tumor material per patient. However, these "amplified" models lack many elements of the human tumor microenvironment (TME), including tumor heterogeneity (particularly the stromal component[2]), molecular transformation events, and drug resistance mechanisms.[3,4] Since PDX mice are immune deficient, testing of immunomodulatory agents is not possible.[2,3] ('Humanized' mice[2] are immune competent but still have rodent-derived stroma.) Also, PDXs from individual patients grow too slow to inform therapeutic decisions. Hence, functional tests with intact TME are critically needed to quickly ascertain the efficacy and toxicity of potential treatments.

In the last decade, functional drug testing technologies based on microscale biomimicry have revealed the power and clinical relevance of *ex vivo* testing of cancer patient tissue. These bioengineered models include organs-on-chips[5] (OOCs), patient-derived organoids[6] (PDOs, also termed patient-derived tumor spheroids or organotypic tumor spheroids, among other terms). However, in these platforms, which often take weeks to months to establish, the tumor tissue is generated *de novo* by growing the patient's cancer cells or by adding separately-derived cells from other patients or from cell lines.[7] Expansion of the tissue has enabled high-throughput testing with biobanking for many tumors[6], and can reveal particular drugs that target key signaling in cancer cells of specific patients.[8] Tissue bioengineering allows for building *de novo* microvasculature into the models, *e.g*. for studying angiogenesis or tumor cell extravasation.[9] Unfortunately, the tissue engineering and/or expansion process also compromises the TME, including the patient's immune microenvironment[6,10] – limiting the general relevance of PDOs and OOCs as models for immunotherapy, since immunotherapy drugs primarily act on the TME.[11,12] These limitations are a fundamental hurdle for the personalization of therapies which need to be customized to the unique TME of the patient,[1] and also for the development of combination immunotherapies, which often target the human TME.[13] The pace of progress in clinical studies puts an additional pressure to developing reliable, quick, and inexpensive drug efficacy tests; immunotherapy clinical trials, especially in combination with other therapies, are exponentially rising in number.[14] In sum, bioengineered models allow for high-throughput drug tests but fail to faithfully recapitulate the patient's TME.

Microscale cancer models based on microdissection, a mechanical approach that separates the tumor into many discrete tissue units without using dissociation enzymes, offer an attractive strategy to preserve the TME intact, maximize the use of scarce biopsies, and minimize the use of animal models.[2,15] Microdissected tumors (µDTs)[16] consist of pieces of tumor that are large enough to preserve the TME *in vitro* and, at the same time, small enough for diffusion alone to ensure their viability[17] and for miniaturized fluid handling.[18–21] µDTs have been tested in various formats, including precision-cut slices (PCTS)[18,22–24] and smaller fragments, which are sometimes referred to as patient-derived

explants (PDEs)[2,25–29] and include patient-derived organotypic spheroids (PDOTS, 40-100 µm-wide).[21,30] Notably, for decades PDE cultures have provided a way to preserve the tumor and its TME (with its native immune cells) within manually cut small (typically ~1-3 mm-wide) pieces. Using single cell RNAseq, LeBlanc et al. showed that PDEs from glioma could retain much of the spatial heterogeneity of tumors.[31] PDEs, PCTS, and PDOTs have shown promise for the study of cancer drugs, including immunotherapy with checkpoint inhibitors, with some demonstrations of predictability with patient outcomes, but at low throughput.[2,15,18,21,24–26,28–30]

Various approaches exist for preparation of µDTs. Microscale tumor fragments are typically created manually by mincing with a scalpel, followed by growth in solution or in a gel such as collagen, sometimes on Transwells[32,33] or in microchannels.[21,30] The use of more precise tools such as a vibratome has already helped improve the microdissection process. Astolfi et al.[16] prepared ~420 µm-diam. cylindrical µDTs by punching cores from PDX tumor slices and manually loading them in microchannels with five traps each. The reproducible size of the punched µDTs allowed for a metabolite transport model[16] and resulted in higher survival rates and lower degree of hypoxia than in PCTS from ovarian and prostate cancer PDXs, indicating an inherent diffusive transport benefit in smaller, higher surface-to-volume ratio pieces.[17] Cordts et al.[34] developed micromachined silicon blade dicers and stainless steel graters that can quickly generate many tumor fragments. Overall, previous microdissection approaches have successfully demonstrated culture of the tumor in the context of its TME, but, until now, do not simultaneously enable higher-throughput tests and maximize the use of precious biopsy tissue.

Motivated by the limited amount of tumor tissue available from each patient (tumors average ~1 cm^3 at the time of intervention[35], with size at diagnosis decreasing due to improvements in early detection techniques[36]), we recently developed a straightforward microdissection technique based on a tissue chopper. The chopper mechanically cuts tumors into thousands of regularly-sized, cuboidal-shaped µDTs (referred to as "cuboids") in ~30 min.[37] Due to their small size, cuboids can be rapidly arrayed using hydrodynamic traps in microfluidic devices (96-well plate with 4 cuboid traps/well)[37,38] or loaded into multi-well plates using a custom robot (up to a 384-well plate, with a programmable number of cuboids/well).[39] In addition to drug tests, cuboids have been applied to label-free aptamer-based electrochemical monitoring of cell death.[40]

Here we characterize the retention and function of the native TME over several days in culture from mouse and human tumor cuboids and demonstrate their suitability as microscale cancer models that can complement existing models. We evaluate the presence of tumor and stromal cells as well as cytokine secretion. In addition to traditional tissue culture platforms, we utilize devices with microfluidic arrays that facilitate 3D imaging and analysis as well as drug testing (schematic in **Fig. 1**A). The regular size of the cuboids enables microfluidic manipulation and analysis.[39] We measure traditional viability drug responses and probe deeper into drug responses by targeted protein profiling of signaling pathways and by global quantitative proteomics. Proteomics provides a complex readout that encompasses molecular responses to drugs, as well as profiling the TME. These results support cuboids as a valuable live tumor model with a rich TME that supports

a wide variety of analysis approaches for deep investigation of drug response for solid tumors in the context of their TME.

Results

Evaluation of cuboids in culture

Our cuboid microdissection technique uses automated and precise cutting in a way that allows us to maximize the yield of similarly sized, TME-retaining microdissected tissues. The technique simultaneously optimizes cuboid viability, cuboid uniformity, and cuboid number, which is maximized due to a cubic power law arising from three orthogonal cuts. Theoretically (if the blade were infinitely thin and did not cause tissue loss), an ideal 1 cm^3 cube of solid tumor would yield 25^3 = 15,625 400 µm-wide cuboids, or 40^3 = 64,000 250 µm-wide cuboids. In practice, depending on the tumor, from an irregular ~1 cm^3 biopsy we obtain over a thousand ~400 µm-wide cuboids and thousands of ~250 µm-wide cuboids due to various losses in the cutting and filtering processes (amounting to >75% loss of the tumor mass), but the cubic power law still holds. Typically, we first prepare tumor slices either with a vibratome (250 or 400 µm) or with a tissue chopper (400 µm) from 6-cm tissue cores (**Fig. 1**B). By geometry, a 400-µm cuboid has ~4.1 times more volume (and thus TME) than a smaller, 250-µm cuboid. From previous work by others on tumor spheroids, we inferred that cuboids larger than 400-µm would result in hypoxic cores.[41,42] We used syngeneic mice (with intact immune systems) for experiments with mouse cuboids. The mouse breast cancer tumors were derived from the Py8119 cell line grown either orthotopically (in the mammary fat pad) or subcutaneously. For mouse cuboids, but not human cuboids, the polygonal shape observed immediately after cutting changed to a spheroid shape by the following day, presumably due to differences in ECM stiffness. To consistently refer to these tissues by how they originated, we term them "cuboids" even if their final shape is spheroidal.

As the cutting process is imperfect and necessarily causes some tissue damage, we evaluated cuboid viability and size variability. We compared two sizes of cuboids (250 or 400 µm) from mouse tumors (**Fig. 1**B).[37] After 3 days cultured in 6-well plates, live/dead staining with SYTOX Green (SG) dead nuclear stain showed very similar high viability of ~90% for both sizes of cuboids (**Fig. 1**C). We approximated the mouse cuboid sizes at day 3, when they had already rounded up, by a diameter estimated from their area from an image. Using a vibratome to precisely cut the tumor into well-defined slices as the first cut, the diameter was 313 ± 48 µm (ave ± SD) for the 250-µm cuboids and 422 ± 58 µm for the 400-µm cuboids, showing a similar coefficient of variation (CV) of 15% and 14%, respectively, for both sizes.

Tumor heterogeneity does not appear to be a factor in cuboid size variability. As expected, patient tumors had more heterogeneity than the mouse syngeneic breast cancer model used. Slices from colorectal cancer metastatic to the liver (CRC-LM) and intrahepatic cholangiocarcinoma (ICC) tumors had clearly visible non-tumor stromal regions and necrotic bloody regions (**Fig. 1**D, **Fig. S1**). Yet we saw similar variability in cuboid sizes between patient cuboids and mouse cuboids. The estimated mean side length of 400-µm human CRC-LM cuboids at day 0 was 493 ± 62 µm (CV = 12.6%, n=252 cuboids, **Fig. 1**E),

with a CV very similar to that observed for mouse (14%). As the dents left on the plastic substrate underneath the slices by the tissue chopper were relatively evenly spaced (400 ± 9.5 µm, CV = 2.4%, see Methods), most of the variability must arise from other factors, such as the initial vibratome slicing, the tumor itself, and processing artifacts (*e.g.*, edge effects). In conclusion, cuboid size variability was similar between the relatively homogeneous mouse tumors and the more heterogeneous human tumors.

The histological heterogeneity of patient tumors suggests that the cuboid viability could vary more than with mouse tumors. For patient cuboids, we assessed viability by RealTime-Glo (RTG) luminescence, which is not affected by the autofluorescence often seen in patient tissues and permits sequential live measurements. We compared 3 different patient tumors and cultured them in different manners (well plate, collagen with air-liquid interface, and in microtraps). We saw a similar percentage of cuboids/wells with strong viability signal (80-98%) (**Fig. S1**). Looking at only the two tumors with one cuboid per well on multi-well plates, we saw low viability (<33% of the mean) in only 6.3% (CRC-LM) and 1.5% (metastatic melanoma, MM) of the cuboids. For these individual cuboids, viability measurements showed similar variability, with a CV of 55% for both the CRC-LM (n=365, day 2) and the MM (n=82, day 1). The CV was 28% higher than in mouse Py8119 breast cancer cuboids (CV = 43%, n=140, day 2). In sum, these experiments confirmed the viability of human patient cuboids and showed that, as expected, it was more variable than what we saw in the Py8119 mouse tumor model.

We also sought to verify that needle core biopsies could provide viable microdissected tissues for culture. In the clinical setting, needle core biopsies, each ~1-2 centimeters long, are commonly used to establish diagnosis and tumor characterization. We obtained six cores from a Py8119 mouse tumor with an 18-gauge needle (838 µm-diam., semi-circular cutting profile) and cut the cores once with the tissue chopper (250 µm). This process yielded 119 semi-circular "discoids" of 250 µm thickness at day 0. Like cuboids from the same tumor type, the discoids evolved into a spheroidal shape by day 3 averaging 377 ± 87 µm in diameter (ave ± SD; **Fig. S2**). The viability (87%) was like that of 300 µm-cuboids prepared in parallel (83% viability; 261 ± 52 µm in diameter). Although we continued our study using cuboids, this result suggests that our methodology could potentially be widely applicable to solid tumors sampled through needle biopsies.

The complexity of the mouse cuboid TME

As tumor explants grow in culture, the cellular makeup of the TME changes over time, presumably from cell growth, cell migration, phenotype alterations, and/or cell death.[18] We evaluated how the TME of Py8119 mouse breast cancer cuboids evolved over the first week in culture because this period provides a sufficient timeframe for functional assays and minimizes the time over which the TME changes. We performed multi-immunohistochemistry (multi-IHC) on thin sections of 400-µm and 250-µm cuboids that had been cultured in suspension in well plates (400 µm: **Fig. 2**A, 250 µm: **Fig. S**3), then quantitated the immunostaining with the image analysis program HALO (**Fig. 2**B). We also compared tumor cuboids that had the same tumor cells (Py8119 cell line) but different TMEs as they were generated in two different locations: orthotopic tumors (mammary fat pad injection, 3 tumors) and subcutaneous tumors (2 tumors). As we obtained similar

results in 400-µm cuboids from both locations (**Fig. 2**B), we plotted individual values and combined results for mean values. Comparison of day 0 to day 3 in 400-µm cuboids showed general maintenance of tissue structure by H&E, followed by shrinkage of the cuboids by day 7. Apoptotic cell death (cleaved-caspase 3, CC3) was minimal initially, limited to necrotic regions from the initial tumor seen at day 0 and a few scattered cells the subsequent days. Apoptosis was present often in the central region at day 3 (~10% of the cells), then decreased at day 7. The apoptosis at day 3 presumably results in the smaller cuboids size at day 7 due to remodeling after cell death. In contrast, the 250-µm cuboids showed minimal apoptosis and did not get smaller over time, as would be expected from their smaller size and the resulting better diffusive transport of nutrients and oxygen compared to the larger 400-µm cuboids. Proliferation (Ki67) in 400-µm cuboids started very high initially, with ~30% of cells at day 0 and day 1, then gradually reduced to ~17% at day 3, but persisted with ~9% of cells at day 7. Proliferation trends in 250-µm cuboids were similar. These general functional markers showed the overall health of mouse tumor cuboids in short-term cultures.

We also measured the presence of specific cell types to explore the dynamics of the cellular composition of the cuboid TME. Endothelial cell staining (CD31) gradually diminished from ~0.7% of the total area at day 0 to 0.5% at day 1, 0.3% at day 3, then to minimal staining at day 7. This rapid disappearance of vascular structures *ex vivo* is a common observation in the absence of circulation.[43] Staining for immune cells (CD45) was strong initially at ~32% of total cells, consistent with the previously reported CD45+ fraction in PY8119 tumors.[22,44] The CD45+ percentage gradually diminished, with 17% at day 1, and gradually decreased to 7% at day 7.

Particular immune cells are known to play specific roles in tumor biology and response to therapies, such as tumor-associated macrophage and cytotoxic T cells.[45] To look at a few of the many specific immune cell types present in the cultured cuboids, we performed an additional 5-plex multi-IHC (**Fig. 2**A,B; **Fig. S3**). We found that tumor-associated macrophage (TAMs, F4/80+) were the most frequent immune cells, which is consistent with flow analysis of cultured Py8119 slices[22] and with a previous study of *in vivo* tumors.[44] TAMs comprised ~43% of the total cells in the cuboids initially, persisting at 27% at day 3 and 19% at day 7. While there appeared to be abundant tumor-associated neutrophils (Lys6G), the weak staining made quantitation not feasible. We also observed scattered T cells (CD3), including some CD8+ T cells, with T cells representing ~2% of cells at day 1, 0.6% at day 3, and 0.2% at day 7. We did not see many natural killer cells (NKp46) in the cuboids (~0.07% of cells throughout), which is consistent with the few clusters of positive cells seen in sections of the initial tumor. We observed similar trends in the 250-µm cuboids, except for ~4-fold fewer TAMs (4.5%) at day 7. Overall, we chose to continue with the 400-µm cuboids to maximize TME representation in each cuboid. We did not perform analysis of rarer cell types for individual cuboids given the scarcity of sampling per cuboid and the small size of cuboids. Despite these limitations, the immunostaining clearly revealed the continued complexity of the cellular TME in cuboids over short-term culture.

Distribution of immune and endothelial cells by 3D immunostaining of mouse cuboids

Within a tumor, immune and endothelial cells are not distributed homogeneously, but their 3D distribution is difficult to assess from isolated 2D sections. To directly evaluate the 3D distribution and heterogeneity of immune (CD45) and endothelial cells (CD31) among individual cuboids, we used a microfluidic device that facilitated 3D immunostaining and analysis of a subset of the intact mouse Py8119 400-µm cuboids used for multi-IHC (**Fig. 2**C-I). The devices featured arrays of hydrodynamic cuboid traps (**Fig. S4**), similar to a device we developed previously for drug testing,[38] but without valves and with rapid fabrication by laser micromachining. Here, the device facilitated culture, immunostaining, clearing, and confocal analysis of the cuboids. Three independent, rectangular wells each had 48 microtraps that connected to one outlet (144 traps total) (**Fig. 2**C,D). To load the device, we used flow to pull a suspension of cuboids in 20% polyethylene glycol (PEG, 8,000 MW) into the traps (200 mL/hr suction). After culture, the cuboids were then fixed, immunostained, optically cleared, and imaged by confocal microscopy while remaining on the device.

3D analysis of cuboids in the traps allowed comparison of cell-type specific staining and cuboid size (**Fig. 2**D-G). We evaluated cuboids from 2 subcutaneous and 2 orthotopic tumors at day 0 and at day 2, as CD31 staining was almost not detectable by day 4. Qualitative assessment by 3D visualization of immunostained surfaces with Imaris (see Methods) revealed abundant CD45 cells at both time points, though less at day 2, and a dramatic reduction in CD31 vasculature at day 2 (**Fig. 2**F). Staining for apoptosis (CC3) revealed scattered positive cells at day 2 (**Fig. 2**G). We did not observe any obvious qualitative differences between subcutaneous and orthotopic tumors (n=2 each). To better understand the distribution of sizes and immunostaining among individual cuboids, we performed a quantitative 3D image analysis for one orthotopic tumor (**Fig. 2**F-I). 3D analysis allowed us to directly measure cuboid volume (**Fig. 2**F), which we used to establish correlations with the fractions of cuboid volume stained by endothelial cell marker CD31 (**Fig. 2**H) and immune cell marker CD45 (**Fig. 2**I). While mean cuboid volume decreased 23% from day 0 to day 2), it was very variable at both timepoints (CV = 36% and 53%, respectively). Over this timeframe, the CD31 volume fraction (**Fig. 2**H) showed a 63% decrease, like the 59% decrease seen at day 3 on 2D sections by multi-IHC (**Fig. 2**B). Most of this decrease in CD31 occurred in the larger cuboids (**Fig. 2**H). The overall 33% reduction of CD45 volume fraction at day 2 was consistent with the amount seen by multi-IHC at days 1 and 3 (22% and 49% respectively, **Fig. 2**B). However, in contrast to CD31, the CD45 volume fraction did not show a dependence on cuboid size (**Fig. 2**I).

The TME and spatial heterogeneity in patient cuboids

In contrast to the relatively homogeneous mouse tumor models such as the Py8119 breast cancer tumors above, patient tumors are known to display large amounts of spatial heterogeneity (*e.g.,* metabolic, cellular, and genetic), both within tumors and between tumors of the same type.[22] Within the patient tumor slices and between cuboids, spatial heterogeneity was readily apparent (**Fig. 1**D; **Fig. S1**). In CRC-LM, regions with high autofluorescence and darkness on brightfield images corresponded to relatively acellular stromal regions (areas presumably a result of post-necrotic fibrosis after neoadjuvant treatment).[18]

The TME of these patient tumor cuboids started as relatively heterogenous, and further changed in culture. We compared multi-IHC of 400-µm cuboids from two types of patient tumors, a CRC-LM and a metastatic melanoma (MM) from a lymph node over a week in culture (**Fig. 3**A,B). For the CRC-LM which had clear subregions of "tumor" (dominated by tumors cells) and stroma, we also performed quantitative analysis of the staining (**Fig. 3**C-G). H&E histology showed some remodeling, with qualitative maintenance of the tumor microstructure. In the CRC-LM, but not in the melanoma, from day 1 onward the tumor cells appeared to form a superficial layer in addition to CRC tumor cells inside, consistent with their epithelial origin and their histology in the metastatic tumor. Despite the remodeling, we found that the relative amount of tumor (versus stroma) remained relatively constant over the week, with around 40% of the area (mean 45%, range 35-53%) and most of the cells (mean 72%, range 60-83%); we defined tumor/stroma subregions using tumor cell staining (AE1/2) and nuclear staining (DAPI) (**Fig. 3**C).

Despite scattered baseline apoptosis (CC3), the central apoptosis we had observed in the mouse tumor was not apparent in either human tumor. Though we could have missed the appropriate time point to catch central necrosis, the relatively consistent size of cuboids over the week suggests that central necrosis had not occurred. Furthermore, we did not observe a marked decrease in cuboid size over time as we had in 400-µm mouse cuboids (**Fig. 2**A). The patient cuboids displayed abundant proliferation (Ki67) at all timepoints, primarily in tumor regions as identified by histology (H&E or DAPI) and by tumor cell markers (partial staining of tumor cells: AE1/2 for CRC and a mix of markers for melanoma). This staining established the continued health (proliferation with minimal cell death) and some structural remodeling of cuboids in culture. We saw similar results in another CRC-LM grown in collagen air-liquid-interface, with an additional correlation of relatively acellular cuboids with undetectable RTG viability (**Fig. S1**).

We observed dynamic changes of specific cell types within cultured cuboids, as shown by immunostaining (**Fig. 3**A,B). In CRC-LM cuboids, clear endothelial cell staining (CD31) slowly tapered off over time, as in mouse. In melanoma cuboids, strong endothelial staining was restricted to an area of the initial tumor, with minimal staining in both day 0 and in cultured cuboids. In CRC-LM initial tumor and cuboids, tumor-associated fibroblast staining (by smooth muscle actin, SMA) clearly colocalized with the relatively acellular, non-tumor, stromal areas. In contrast, in melanoma tumor and cuboids, SMA staining demarcated smooth muscle cells that surrounded CD31-positive blood vessels.

We observed a very uneven distribution of immune cells in the initial tumors and in the cuboids, as demonstrated by general staining for immune cells by CD45. To assess the distribution of select immune cell types in the cuboids, we performed multi-IHC for macrophage (CD68), T cells (CD3), and CD8+ T cells. In contrast to the Py8119 mouse breast cancer tumor staining, which had a predominance of macrophage with few T cells, human tumors and cuboids had relatively few macrophages and many T cells. In the melanoma, most of the T cells were CD8+, with very large numbers in some cuboids and few to none in others. The overall heterogeneity of the immune cell staining between cuboids suggests that individual cuboids could be very different from each other, notably in tumor content for CRC-LM and in immune cell content for the melanoma. The results in the CRC-LM

cuboids were consistent with findings from a 25-plex multi-IHC study of the immune microenvironment in CRC-LM.[46] The melanoma cuboid staining and histology appeared to conform more to the melanoma tumor which had invaded the lymph node than to the normal morphology of a lymph node, though further immunostaining could better distinguish the components and structure of lymph nodes. In sum, over a week in culture, the patient cuboids maintained the tissue complexity and heterogeneity of the initial tumors, including continued cell proliferation and a diversity of cell types.

Heterogeneity of human cuboids by 3D immunostaining

The greater amount of heterogeneity by 2D immunostaining and viability in patient cuboids makes 3D investigation of spatial heterogeneity particularly important. Lightsheet microscopy of whole-mount pseudo-H&E staining of a CRC-LM biopsy and cuboid highlight the variability of the histology both at distant regions and within the dimension of a single cuboid (**Fig. 3**H). In 3D immunostaining experiments on patient cancer cuboids (**Fig. 3**I,J), we looked at immune cell (CD31) distribution as well as at apoptotic cell (cleaved-caspase 3, CC3) distribution, given the larger amount of starting cell death compared to mouse. We used cuboids from one CRC-LM tumor (day 0 only) and one idiopathic cholangiocarcinoma (ICC) tumor, a primary liver tumor (day 0 and day 4). We loaded the ICC cuboids into a microtrap device, then processed either immediately after loading (day 0), or after 4 days in culture. This device had a single chamber with 96 traps and a single outlet. Given tissue scarcity, to ensure loading of one cuboid per trap we used manual guidance of individual cuboids (visualized with a microscope) in addition to hydrodynamic flow. For the ICC cuboids, RTG luminescence confirmed the viability of the cuboids (**Fig. S1**).

The patient cuboids were markedly more heterogeneous than the mouse cuboids, including in the amount of tumor (regions with many nuclei) versus non-tumor tissue (regions with very few nuclei). In contrast with mouse cuboids that showed minimal initial cell death (after elimination of necrotic areas during preparation before slicing), patient cuboids displayed multiple regions of cell death even at day 0 in CRC-LM (**Fig. 3**I) and in ICC (**Fig. 3**J); many cuboids had very few, well-spaced cells, likely consisting of mostly connective tissue. There was some increase in CC3+ apoptotic cell death at day 4 in the ICC cuboids. At day 0 for both tumors, the CD45+ immune cells were present variably and in clusters, as had been seen by multi-IHC for other tumors (**Fig. 3**A,B). At day 4 in ICC cuboids, immune cells were still clearly present with no significant difference in mean volume from day 0 (**Fig. 3**J,K). Furthermore, unlike in mouse, mean cuboid volume did not significantly change (**Fig. 3**K), consistent with the qualitatively similar cuboidal shape seen in 2D images (**Fig. 1**) and in histological sections (**Fig. 3**A,B). This immunostaining confirms at the whole cuboid level the continued presence of immune cells and other cell types in culture for ICC, as shown by 2D multi-IHC for CRC-LM and metastatic melanoma.

Cytokine and chemokine secretion in cuboids

Cytokines, including a large family of chemokines, secreted by both tumor and stromal cells, play key roles in the progression, diagnosis, and prognosis of cancer.[47] Other studies have examined cytokine secretion in relation to immunotherapy for PDEs/PDOTs.[28,48] For

cuboids, we found abundant expression of cytokines and chemokines in the supernatant of mouse and human cuboids grown in U-bottom 96-well plates with multiple cuboids per well (**Fig. 4**). Luminex measurement of Py8119 breast cancer cuboid supernatant revealed baseline expression of 31 of a panel of 32 cytokines/chemokines (**Fig. 4**A). Expression of multiple molecules normally secreted by the innate immune system (*e.g.,* G-CSF, IL-6, and TNFα) is consistent with the large presence of macrophages seen in cuboids by immunostaining above. CXCL10 may be produced by monocytes, endothelial cells, and fibroblasts. The interferon-gamma (IFNγ) and IL-2 signal is consistent with the low presence of T cells in cuboids by immunostaining and by previous study in slices.[22] Application of lipopolysaccharide (LPS) for 24 hrs to stimulate the innate immune system led to expected increases in inflammatory cytokines, IL-1α and TNFα, and chemokines CCL3, 4, and 5 (**Fig. 4**B).

Cytokines, especially chemokines, have been implicated at all stages of colorectal cancer, including metastasis and recruitment of immune cells.[49] In supernatant from patient CRC-LM cuboids (**Fig. 4**C), we detected clear expression of 29 cytokines and other secreted molecules of interest at baseline (nELISA on a panel of 192 secreted molecules), most at >10 pg/mL. For example, IL-8 is a key pro-inflammatory pro-tumor chemokine[50] (84 pg/mL). CCL2 is a small chemokine that recruits CCR2+ tumor-associated macrophages to sites of liver metastasis and is associated with a poor prognosis in CRC (15.6 pg/mL). Enhanced expression of CXC chemokines such as CXCL10 (173 pg/mL) is associated with poor survival and prognosis in most human cancers including CRC, making these molecules potential biomarker candidates.[47,49] Other non-cytokine signaling molecules included high levels of Trem2 (Triggering receptor expressed on myeloid cells; ~4,189 pg/mL), a secreted receptor expressed in TAMs that is associated with a tumor-suppressive microenvironment and also offers an attractive therapeutic target.[51] These cytokines support the use of cuboids as a model system for CRC-LM with native expression of cytokines/chemokines critical to the immunomodulatory crosstalk between tumor and immune cells.

Drug treatment of mouse cuboids

As a first demonstration of drug responses in mouse cuboids, we treated Py8119 cuboids from a subcutaneous mouse breast cancer with 2 drugs using a 24-well microdevice with 96 microfluidic traps (**Fig. 5**A-G). Each microfluidic trap contained up to 3 cuboids, with 4 traps per well. We used one device per condition: the cytotoxic chemotherapy drug, cisplatin (CP), the broad-spectrum protein kinase inhibitor staurosporine (STS), or a no-drug control. We measured viability by RTG luminescence before and after 3-day treatment. By immobilization of the cuboids in fixed and separated locations in an array, the device facilitated analysis of viability by luminescence for individual traps. We observed significant responses to both CP and STS (**Fig. 5**H). Similar responses were seen using a Py8119 tumor grown orthotopically, using a device with three regions of 48 traps each (**Fig. S5**). While these microfluidic devices do not allow for parallel evaluation of multiple drugs within a device (the wells are fluidically connected), we have developed a valved 96-well version of these microtrap devices that allows for testing unique drugs in each well.[38] While the present viability readout does not have enough resolution to discern

between the different cell types, future improvements in the technique might allow a simultaneous readout of the viability of non-cancerous cells, or treatment of normal tissue in parallel as an assessment of the toxicity of the treatment.

Because of the genetic heterogeneity of tumor cells and the non-homogeneous distribution of tumor and TME cells in a tumor, we expected the drug responses to also vary from cuboid to cuboid. To look at the variability of the drug response at the level of individual cuboids, we manually pipetted single mouse Py8119 cuboids from the same tumor into a 384-well plate and treated with the same drugs in parallel (**Fig. 5**I-K). As in the microdevice, the addition of CP and STS resulted in a strong decrease in viability (RTG) and an increase in cell death (SG fluorescence) (**Fig. 5**L). Despite the relative homogeneity of the mouse Py8119 tumor, there was some variability in the viability before drug treatment and after culture for the control conditions. Using the standard deviation values observed from these drug treatments, power analysis (80% power and α=0.05) estimated that, to detect a 50% change, we would need at least 2 cuboids for SG and 5 for RTG, and to detect a 30% change, we would need at least 4 cuboids for SG and 12 cuboids for RTG. We expect that the number of cuboids needed for each condition with more heterogeneous tumors, especially with human patient tumors, would be much greater.

Cuboid responses to kinase inhibitors and to checkpoint inhibition

Functional drug testing on cuboids could help address the lack of efficacy of targeted therapies on many cancer patients who are candidates by their genetic profile of their tumors. Protein kinase inhibitors are a large class of drugs that are often used as targeted therapies for cancer. To demonstrate the suitability of cuboids for drug screening, we tested a panel of 35 kinase inhibitors on mouse Py8119 cuboids in a standard 96-well plate format (**Fig. 5**M). With a multi-pipettor, we manually pipetted a random number of cuboids into each well, which resulted in 2-6 cuboids per well. After measuring the pretreatment viability by RTG luminescence, we removed high and low luminescence outliers to reduce the variability of the starting condition. We measured the drug responses before and after 3 days of drug treatment, relative to the DMSO vehicle control. For 17 of the drugs, we saw >50% reduction in viability compared to DMSO control, and 9 showed ≥75% reduction. The relatively high concentration used (500 nM) may contribute to the responses to many of the tested drugs. The high reproducibility of the responses for duplicate wells for Py8119 breast cancer cuboids for this experiment contrasts with the variability seen in the single cuboid experiments with the same tumor type. We attribute this difference to both the use of a pool of cuboids per well here, as well as to the exclusion of wells with unusually high or low pretreatment luminescence. Testing multiple cuboids per well appears to reduce noise and minimize reagent use, and thus could facilitate higher-throughput drug testing approaches in some situations.

We also tested cuboids with checkpoint inhibitor immunotherapy drugs, which have been previously shown to act in other µDT formats,[2,32,48] even identifying features predictive of patient response.[28] As a proof of concept, we applied the PD-1 checkpoint inhibitor to cuboids from a subcutaneous MC38 mouse colon cancer, which is known to respond to checkpoint inhibitors *in vivo*[52] and in bulk culture of microdissected tissues in collagen[30,32] (**Fig. 5**N). Checkpoint inhibitors remove the suppression on CD8+ T cells, permitting the T

cells to attack and kill the target cancer cells. Given the greater variability in responses to checkpoint inhibition compared to in responses to kinase inhibitors, we tested multiple wells for each condition, each with 6-12 cuboids per well. After four days exposure to PD-1, we saw both a decrease in viability of ~40% in comparison to IgG control, as well as a ~2-fold increase in IFNγ, a sign of activation of the immune system. This simple test confirms that cuboids could be used as immunotherapy drug evaluation platforms.

Drug evaluation with patient cuboids

One defining test of the clinical relevance of a cancer model is to provide data about the efficacy of existing drugs, as would be appropriate for personalized treatment evaluation. Using cuboids from the same CRC-LM tumor as in Fig. 3, we used a custom robot[39] to facilitate the transfer of large numbers of individual cuboids into a 384 well plate for drug response evaluations (**Fig. 6**A-G). The patient had undergone chemotherapy prior to resection, including one cycle with FOLFOX, a combination of folinic acid, 5-fluorouracil (5-FU), and oxaliplatin. As seen in tumor slices (**Fig. 1**D) and cuboids (**Fig. 3**A), the CRC-LM tumor had regions that correspond to relatively acellular stroma as described before,[18] likely due to post-treatment necrosis. Putative stromal cuboids showed bright green autofluorescence, and cuboids with blood (red in light), appeared relatively dark areas in the green channel (**Fig. 6**A). We note that the same regions may also contain tumor cell areas, as the slices and cuboids were relatively thick (400 µm), and the tumor and stroma may be quite interspersed, as seen on H&E (**Fig. 3**A). We measured viability (RTG) before drug application (day 2), then after 3 and 5 days of drug exposure. Treatments consisted of either the standard chemotherapy regimens FOLFOX or FOLFIRI (a combination of 5-FU and irinotecan), staurosporine, DMSO vehicle control, or a no-drug control. As an additional cell death readout, we measured cell death with propidium iodide (PI, a red nuclear cell death indicator), after 5 days of drug exposure (day 7, end of the experiment).

In the CRC-LM cuboids, we observed both a decrease in viability (RTG) and an increase in cell death (SG) at day 7 to FOLFOX and FOLFIRI, two first-line treatments for colorectal cancer,[53] along with STS control. The small overall reductions in viability for FOLFOX (20%), FOLFIRI (24%), and the STS positive cell death control (30%), may reflect the heterogeneity of the cuboids. However, the responses were highly significant despite the clear heterogeneity in the baseline signal, in the changes to control and DMSO treatments over time, and in the drug responses. Power analysis estimated that we would need to test 25 cuboids to detect the 24% decrease with FOLFIRI, and 18 cuboids for the 30% decrease with STS (81% power and α=0.05). These experiments show that we could assess responses to patient chemotherapy drugs in individual cuboids, finding an overall response to therapies with enough cuboids.

As we showed with mouse cuboids and kinase inhibitors, one way to reduce the variability and number of wells per condition is to combine multiple cuboids per well, which affects the consumption of tumor and reagents per experiment. In cuboids from a biopsy from a patient with metastatic melanoma in an inguinal lymph node (multi-IHC in **Fig. 3**), we compared drug responses between wells with one or eight cuboids each (**Fig. 6**H-K). The patient's tumor had progressed after initial response to checkpoint inhibition in the past and had recently responded to a BRAF inhibitor. After manual transfer of either 1 or 8

cuboids per well of a 96-well plate, we applied drugs at day 1 for 6 days and measured viability by RTG. The treatments were an anti-PD-1 checkpoint inhibitor, its IgG control, cobimetinib (a clinically approved MEK inhibitor), STS (a multi-kinase inhibitor used as a positive cell death control), or a no-drug control. We saw no response to checkpoint inhibition, consistent with this patient's treatment history.

On the other hand, we saw a clear response to cobimetinib (~30% decrease) and STS (~50% decrease for 8 cuboids/well and a ~65% decrease for single cuboids) by 3 days of treatment (**Fig. 6**J,K). The response to the MEK inhibitor cobimetinib is consistent with the tumor's sensitivity to treatment with binimetinib, a BRAF inhibitor. As would be expected, the cobimetinib response was more clearly seen with 8 cuboids per well, with about half as much variability in the drug response (15% vs 32%) and in the baseline viability (26% vs 55%), and a more statistically significant drug response at the earlier time point compared to 1 cuboid/well. However, we still saw a response with only 1 cuboid/well, using half the total tissue, but 4 times more reagent. Power analysis of the cobimetinib drug response with 8 cuboids/well determined a minimum of 2 wells (for a total of 16 cuboids), whereas with 1 cuboid/well, determined a minimum of 8 wells (but only a total of 8 cuboids). We note that the numbers of cuboids needed would be higher with a weaker or more variable response, as with the CRC-LM above. This optimal number of samples would need to be decided for each application. In sum, these experiments with two tumor types showed that patient-derived tumor cuboids exhibit drug responses consistent with the patient's clinical course.

Proteomics of drug-treated mouse cuboids

Over the last decade and largely driven by the efforts of NCI's Clinical Proteomic Tumor Analysis Consortium (CPTAC), mass spectrometry (MS)-based proteomics has provided profound insights into the molecular mechanisms, diagnosis, prognosis, and treatment of various types of cancer.[54] Discovery proteomics pipelines can now achieve very high (femtomole) sensitivity for thousands of proteins in low input samples such as individual organoids[55] or even single cells.[56] However, the massive efforts by the CPTAC have been undertaken on frozen samples (without culture) and do not provide functional information on drug responses. Recently, the combination of proteomics with microdissection techniques or "microscaled proteomics"[57] has permitted evaluation of drug responses on sequential core needle biopsies pre- and post-treatment. Proteomics of drug-treated cultured explants (~1 mm^3) derived from patient prostate cancers helped reveal some of the underlying molecular and cellular changes underlying the drug response[58] and suggested the power of application to even smaller tumor pieces such as cuboids.

To provide a deep molecular readout of both drug-induced changes and the state of the TME at once, we adapted a "microscaled proteomics" workflow to the analysis of cuboids (**Fig. 7**). We treated cuboids from Py8119 orthotopic mouse breast cancer tumors in 6-well plates for 3 days with several drugs including kinase inhibitors. Treatments included the drugs clinically used for cancer: cisplatin (100 µM), paclitaxel (a cytotoxic chemotherapy microtubule inhibitor; 10 µM), crenolanib (a PDGFR inhibitor; 0.5 µM), and regorafenib (a VEGFR inhibitor; 0.5 µM); as well as doramapimod (a pan p38 MAPK inhibitor used for some autoimmune diseases; 0.5 µM) and a DMSO (0.1%) vehicle control. We prepared

samples from replicates of 4 cuboids each, including no treatment (day 4) and pretreatment (day 1) controls. We analyzed the samples by data independent acquisition (DIA) mass spectrometry. With this approach, we consistently identified over 50,000 precursors and 4,000 proteins per sample across treatments using the equivalent of 1 cuboid per injection (**Fig. S6**A). The DIA strategy also afforded high reproducibility (Pearson r>0.95) and precise protein quantifications (median CV<10%) across drug treatments (**Fig. S6**B).

Analysis of the expression of select cancer and TME-relevant proteins from day 1 cuboids demonstrated the ability of the proteomics assay to reveal similar information as other assays such as immunostaining, viability, and cytokines, but with multiple types of markers at once (**Fig. 7**A,B). Among others, we quantified multiple proteins involved in cytokine and chemokine activities (**Fig. 7**A), as well as several TME markers (**Fig. 7**B).[59] These TME markers included proliferation (Ki67) and apoptosis (CC3), key measures of drug response; CD68, a macrophage marker; MRC1 (CD206), a marker of M2 macrophage; PTPRC (CD45) a general marker for immune cells; and VME (vimentin), a marker for tumor cells and the epithelial-mesenchymal transition. Although this approach does not have the cellular resolution of immunostaining or the sensitivity of Luminex cytokine measures, in one test it can evaluate death, proliferation, cell types, and signaling using thousands of target proteins. These proteomic measures could potentially provide a metric of TME heterogeneity that distinguishes each cuboid.

We also examined the effects of the different drugs on the cuboid proteome. Measures of similarity of protein abundance by Pearson correlations across replicates (**Fig. 7**C) and clustering analysis (**Fig. 7**D) revealed that cuboid proteomes undergo substantial and reproducible remodeling in response to drug treatments. As expected, principal component analysis (PCA) to compare the overall similarity in the protein abundance patterns between groups detected a clear difference between day 0 (untreated) and day 3 (treated) cuboids. Paclitaxel, a cytotoxic microtubule inhibitor, seemed to elicit the most dramatic proteome changes in cuboids as reflected by the cluster separation in the PCA (**Fig. 7**D, yellow dots). Crenolib also appeared to cause changes in the proteome relative to DMSO, but to a smaller extent. As shown by a “volcano plot” that visualizes all up and down-regulated genes, we identified expected patterns of drug action from paclitaxel treatment, with decreased proteins related to actomyosin structural reorganization and upregulation of proteins related to activation of the innate immune system (**Fig. 7**E). With Gene Ontology enrichment analysis (**Fig. 7**F), an unbiased method to identify significantly modulated biological processes using the known associations of assigned gene sets, we evaluated the regulated genes between DMSO and Paclitaxel treated samples (**Fig. 7**F). Activated processes included multiple immune-related processes and “response to chemical stimulus”; suppressed processes included double stranded-break repair and Ras signal transduction. This proteomic analysis of small numbers of cuboids demonstrated the potential for rich molecular assessment of cuboids both at baseline and after drug treatment.

Profiling changes in signaling pathways from drug treatment in mouse cuboids

Assessment of dynamic changes in the activation of protein kinase signaling pathways within cuboids could provide focused, immediate insight into drug action. To complement the unbiased protein analysis by mass spectrometry, which detects thousands of proteins in cuboids, we next focused on identifying post-translational modifications in key growth factor signaling proteins. For this purpose, we used the established reverse phase protein array (RPPA) assay, which relies on cuboid extracts and phospho-specific antibodies to detect changes in protein activity.[69] By applying RPPA, we can accurately identify and quantify post-translational modifications and protein activity changes, even in low-abundance proteins, thus enhancing our understanding of protein dynamics within the TME.

We used reverse-phase protein array (RPPA) to look at dynamic changes in signaling pathways in mouse cuboids with drug treatment (**Fig. 8**, **Table S2**). Py8119 breast cancer cuboids were probed with antibodies to look at the activity of 48 proteins, primarily by the phosphorylation state of kinases and kinase-associated proteins, which have critical roles in cancer biology and targeted therapy treatment.[60] Cuboids were treated for 3 days with cisplatin (10 and 100 µM), doxorubicin (an anthracycline cytotoxic chemotherapy drug, 10 µM), STS (2 µM), or DMSO vehicle control. Two samples of ~10 cuboids each were probed with 48 antibodies, and 23 yielded high-quality signals. The corresponding 23 proteins revealed distinct protein correlations, functional protein-protein interactions (physical and predicted), and enriched biological processes from gene enrichment analysis. Six proteins of interest showed differences between drug treatments and DMSO (**Fig. 8**A,B). Phospho-histone H2A.X (p-H2A.X), a marker of DNA damage, was elevated in some of the drug treatments relative to controls, with loss in high dose cisplatin and in staurosporine potentially due to excessive cell death lowering the signal. A strong reduction in phosphorylation of ERK, MLC2 (myosin-light chain) and BAD (a pro-apoptotic and metabolism regulator) was seen in all drug treatments, consistent with their known involvement with cancer processes (*e.g.,* p-MLC2's implication in cell proliferation and cytokinesis, tumor progression and the interaction of tumor cells and tumor associated macrophages). Similarly, p-MDM2, a negative regulator of the p53 tumor suppressor, was reduced in the highest concentration of cisplatin and STS only. Other protein signals were unchanged such as LDHA, a monomer of lactate dehydrogenase. Results from the 23 proteins of interest were used to create a Pearson correlation matrix (**Fig. 8**C) which measures the similarities of patterns between protein signals with respect to the different treatments. We then created a proposed protein-protein interaction network informed by these experimental responses to drug treatment and published data (**Fig. 8**D). This potential insight into the protein signaling networks involved could be followed up with more targeted studies that confirm changes and determine in which cell types they occur.

Finally, gene enrichment analysis of the positively correlated proteins (**Fig. 8**E) yielded the top biological processes predicted to be involved with these drug treatments. These processes included regulation of apoptosis, transmembrane receptor protein tyrosine kinase signaling pathway, regulation of telomerase activity, and regulation of telomere maintenance. The network of proteins that were substantially downregulated in response to chemotherapy includes receptor tyrosine kinase, such as MET, cytosolic effector proteins like MEK, SRC, FAK, and S6, as well as cytoskeletal proteins such as RAC1. This is

particularly interesting because Py8119 is a triple-negative breast cancer (TNBC) model known to be driven by the c-MET pathway.[61] In the majority of TNBC tumors, c-MET is overexpressed, making it a critical driver of cancer progression in these models.[62] The downregulation of these key proteins in response to chemotherapy suggests a potential mechanism by which the treatment exerts its effects and highlights the importance of the c-MET pathway in the pathology of TNBC. This insight could be valuable for developing targeted therapies aimed at inhibiting the c-MET pathway, potentially improving treatment outcomes for patients with TNBC.

Discussion

Cancer models based on cuboids complement other forms of current *ex-vivo* cancer drug tests, with advantages and limitations. We showed that, like other µDTs, cuboids from syngeneic mouse tumor models and human tumors retain a complex TME that makes them suitable as *ex vivo* cancer disease models for functional drug and immunotherapy evaluations. Multi-IHC of mouse cuboids over a week in culture revealed continued proliferation and persistence of key cell types including immune cells. 3D immunostaining of endothelial and immune cells showed the heterogeneity of the cuboids. This relatively intact original TME attributes make cuboids complementary to some of the cancer disease models. PDXs mix human tumor cells with mouse TME, though offer an intact organism; patient-derived organoids (PDOs) and organ-on-a-chip approaches (OOCs) have much reduced complexity, though offer more reproducibility and higher throughput. As for models with an intact TME, cuboids (and PDEs/PDOTs), as compared to tumor slices, allow for much higher throughput in testing and benefit from additional surface-to-volume ratio for improved diffusive mass transport (which reduces hypoxia conditions).[17] However, PDEs/PDOTS have relatively low throughput and inconsistent sizing compared to cuboids. While (growth-based) organoids allows for high-throughput drug screening along with biobanking,[63–65] cuboid testing provides a more suitable cancer disease model for TME-dependent drug evaluations of a small number of drugs. In addition to fast, straightforward preparation without expansion, cuboids could be cryopreserved for later tests as done by others for PDEs[26] and PCTS.[66] In principle, the microdissection process could be improved to yield more cuboids per unit volume using sharper, thinner, and/or micromachined[34] blades. However, unlike organoids, cuboids and PDEs are inherently limited to solid tumors that can be cut and sliced. Also, compared to organoids (with expansion), cuboids are limited by the amount of tissue in the tumor biopsy, which means that the smallest biopsies, such as core needle biopsies, would provide enough tissue for more limited testing. Cuboids that float due to fatty content (*e.g.*, in less differentiated breast cancer) could be more difficult to manipulate. This challenge could be addressed by embedding the cuboids in collagen, shown for CRC-LM cuboids here (**Fig. S1**) and used for microdissected tissues by others.[21,30] In principle, any solid tumor for which PDEs or PCTS have been published should be amenable to preparation as cuboids, including breast, colon, prostate, head and neck, and lung for patient tumors.[2,15]

While the more intact TME of a cuboid makes it a closer biomimic than an organoid, it is still not entirely physiological. The microdissection process itself may cause an acute, transient activation of inflammatory pathways, as has been shown for PCTS of some

normal tissues.[2] The cuboid TME clearly evolved in culture as evidenced by immunostaining. As observed in PDE cultures, multiple challenges exist for maintenance of the original TME *ex vivo*: mass transport limitations (oxygen, nutrients), preservation of the immune compartment, a suitable external support matrix (*e.g.,* hydrogel-mediated retention of immune and stromal components), and optimization of the culture medium composition.[2] Future modifications to optimize culture conditions, such as done by Neal et al.[32] adding IL-2 or by Majumder et al.[29] using patient-derived ECM, could improve maintenance of cell types. In principle, specialized incubation and perfusion setups (such as macroscale or microscale bioreactors[2]) could provide more precise control of oxygen levels and metabolism. As the cuboid microscale model lacks functional vascular structures, oxygen and nutrient delivery to the cells of each cuboid relies on diffusive mass transport. Recently, the successful vascularization of microscale tumor models by several groups, using a reconstituted human TME[9] or PDEs,[67] suggests that a similar approach might vascularize cuboids *de novo*. Even in the absence of circulation, the quantitative reproducibility of diffusive processes at small scales remains an invaluable experimental tool. The microscale size of spheroids, for example, has been used to control and recapitulate hypoxic gradients and necrosis.[68]

Like organoids (PDOs, PDOTS) and PDEs, cuboids are indicated for short-term drug testing studies, with several advantages as well as limitations. We demonstrated the suitability of cuboids for drug testing by evaluating the efficacy of 35 different kinase inhibitors in PY8119 mouse breast cancer cuboids, a checkpoint inhibitor on MC38 mouse colon cancer cuboids, as well as small panels of clinically relevant drugs in cuboids from two types of human tumors. Cytokine secretion from mouse and human cuboids further supported the functionality of the immune and tumor cells in cuboids. This evaluation confirmed that cuboids could model tumor responses to various treatments, including immunotherapies, much like has been shown by others for other µDTs.[2,28,30,32] In combination with our low-cost, high-throughput robotic system,[39] we have the capability to potentially test hundreds of drugs using tissue from a single surgical resection of a patient tumor. Drug treatment of individual mouse and human cuboids demonstrated the amount of heterogeneity in the responses by both viability and cell death assays. Treatment of cuboids in groups facilitated testing a drug panel, such as might be applicable to personalized medicine scenarios. The higher the heterogeneity of responses, such as with patient tumors, the more cuboids would be needed per drug to determine the overall net effect. The use of more cuboids per well would streamline the testing of a larger number of conditions, but at the cost of losing the signal from individual cuboids and their heterogeneity. Though we only looked at acute responses to drugs over several days, and tumor responses in patients occur over months, such studies could still provide critical insight into drug action in that particular tumor. Naturally, elucidation of the clinical significance of drug responses in these tests would require further study with clinical correlations. Finally, outside of drug responses, as with the intense exploration of organoid- and OOC-based models[69] for tumor development, extravasation and metastasis, cuboid-based models could potentially be applied to more fundamental questions in cancer biology.

Our drug response assays (RTG for viability and/or SG for cell death; bulk proteomics; RPPA) could only measure bulk effects but were informative choices given the challenges

associated with measuring large numbers of intact, thick tissues. Overall, a combination of mass spectrometry-based proteomics and targeted analysis of signaling events using RPPA can provide a rich analysis of dynamic proteome changes in response to treatments. This integrated approach can yield valuable insights into the molecular mechanisms underlying treatment responses, potentially guiding the development of more effective therapeutic strategies. With only these readouts, we could not directly discriminate effects on the cell types or obtain correlations with the individual cuboid's stroma or tumor cell content. Not knowing which cells caused the response makes interpretation of partial responses on bulk readouts (*e.g.*, 30% reduction of viability seen for the CRC-LM) ambiguous. However, cell-type-specific assays exist, such as luciferase expression in mouse tumor cells, or cytokine readouts, such as the IFN-γ secretion shown here. Confocal live imaging of cuboids could enable the inspection of the interior of live cuboids with fluorescently labeled cells (the limitation of light penetration could be addressed by multi-photon imaging), but with the disadvantage of very low throughput. One could image immunostained cuboids (cleared and fixed by confocal microscopy as done with untreated cuboids here), to localize a variety of cell markers inside cuboids at cellular resolution, though at too slow and low throughput to combine with higher throughput drug screening. Although the deeper insight offered by proteomics and RPPA did not have single-cell resolution, further studies could localize specific target changes to particular cell types, *e.g.*, with immunostaining or single-cell RNAseq, as has been explored for other PDEs.[2,31]

Further developments of "microscaled proteomics"[57] for cuboids and other PDEs could enable more sensitive and informative single cuboid analysis, providing molecular maps of individual cuboids with cell-type information, as well as both unbiased and targeted drug response readouts. Such individual cuboid proteomic analysis could more directly address the expected link between spatial heterogeneity across the tumor and heterogeneous drug responses.[70] MS-based proteomics is commonly regarded as an expensive technique that is not suitable for multi-well analysis. However, isobaric labeling, *e.g.*, using Tandem Mass Tags (TMTs),[71] a widely used technique for protein quantification by MS, allows for multiplexing and high throughput. With simultaneous quantification of thousands of proteins across multiple samples in a single analysis, TMT labeling has become the approach of choice by the CPTAC to characterize tumor proteomes,[72] and could provide a key advance towards scaling up analysis to single cuboids. A complementary development would be the application of targeted proteomics to cuboids (in addition to the unbiased discovery proteomic screen presented here). Targeted proteomics could possibly achieve even greater (attomole) sensitivity and precision quantification of subsets of proteins of interest,[73] markers of cell composition or immune response[74] and proteins in pathways relevant for tumor biology.[75] While immunohistochemical (IHC) imaging provides the ability to localize and detect very rare cells,[76] proteomics provides superior and unbiased depth and quantitative capabilities, with measurements of hundreds of proteins at once instead of a handful for IHC.[73,77] Targeted proteomics could be leveraged to find key markers of interest, including drug response markers (for more sensitive or rapid analysis) or cell type markers (for understanding the cellular heterogeneity of the tissue).

Together, this data supports the potential for cuboids as a model system to help bridge the critical gap for cancer biology and cancer drug testing between organoids (which have

high throughput and lack TME) and human patients. Cuboids represent a way to optimize the preparation and utilization of micro-dissected tissues (PDEs and PCTSs). Like organoids, cuboids can be integrated with many modalities of assays,[40,78] allowing researchers to tailor experiments with cuboids to help tackle outstanding problems in cancer biology and clinical oncology.

Materials and Methods

Cell Culture

The Py8119 syngeneic mouse breast adenocarcinoma cell line (American Type Culture Collection (ATCC), CRL 3278) was grown in DMEM/F12 (for subcutaneous injection) or F-12K (for orthotopic injection) supplemented with 5% fetal bovine serum (FBS) and 1% penicillin/streptomycin. The MC38 syngeneic mouse colon carcinoma cell line (Kerafast, ENH204-FP) was cultured in DMEM supplemented with 10% FBS and 1% penicillin/streptomycin. Tissue culture reagents were obtained from GIBCO, ATCC, or Fisher.

Tumor Generation for Mouse Model

Mice were handled in accordance with institutional guidelines and under protocols approved by the Animal Care and Use Committee at the University of Washington, Seattle or by the Fred Hutchinson Cancer Research Center. Mouse syngeneic tumor cell lines (Py8119 and MC38) were injected into C57BL mice (Jackson Laboratories), >6 week old female (Py8119) or male (MC38) mice. 1-2 x 10^6 cells were injected subcutaneously (Py8119) or orthotopically (MC38, splenic injection) in Matrigel (Py8119, Corning). Tumors were harvested at < 2 cm^3. If not used immediately, the tumor was stored up to overnight in Belzer-UW cold storage medium (Bridge-to-Life Ltd).

Human Tissue

Human tissue was obtained with written informed consent and treated in accordance with Institutional Review Board approved biorepositories at the University of Washington, Seattle. De-identified tumors were freshly procured and processed for slicing the same day as the resection. Patient 1 was a 40 year-old male with metastatic colorectal carcinoma to the liver that was responsive to neoadjuvant treatment. Patient 2 was a 66 year-old female with untreated cecal adenocarcinoma and a liver metastasis from which we obtained a biopsy. Patient 3 was a 43 year-old male with colorectal carcinoma metastatic to the liver, after being off chemotherapy for a year. Patient 4 was a 70 year-old female with untreated intrahepatic cholangiocarcinoma. Patient 5 was a 29 year-old female with rectal cancer with recurrent metastasis to the liver, after initial treatment with CAPOX (capecitabine and oxaliplatin) followed by only one cycle of FOLFOX 2 months. Patient 6 was a 38 year-old female with widely metastatic melanoma that had progressed after initial response to checkpoint inhibition (anti-PD-1 and anti-CTLA-4). The tumor had a VPS54:BRAF fusion and responded to the BRAF inhibitor binimetinib prior to the inguinal node biopsy.

Cuboid Generation and Culture

After removing necrotic regions from the tumors, we generated cuboids as previously described.[37] For human tumors, and if specified for mouse tumors, slices were cut using a Leica VT 1200 S vibrating microtome or MZ5100 vibratome (Lafayette Instruments) after embedding tissue punches (6 mm diameter, Harris Uni-Core) in 1-2% low-melt agarose. Otherwise, we cut small pieces of tissue into slices using a tissue chopper (McIlwain) after attaching the tissue to a poly(methyl methacrylate) (PMMA) disk with a thin film of cyanoacrylate glue. We cut slices into cuboids with the tissue chopper, then gently dissociated the cuboids with a transfer pipette. The tissue chopper can be used for all three cuts in sequence (including the first cut) to reduce the duration of the procedure, but at the cost of higher variability in cuboid sizes. To measure the variability attributable to the chopper, we measured the distance between the indentations left by the blade on the PMMA disk after cutting 400 µm-wide cuboids (image analysis by FIJI). For 400-µm mouse cuboids, we filtered their suspension through a 750 µm filter (Pluriselect) to remove large fragments followed by filtration through a 300 µm filter (Pluriselect) to remove small debris. To remove potential contamination introduced during the chopping procedure (performed outside the hood for mouse cuboids) we transferred the cuboids to a 100 µm cell strainer (Corning or Falcon) and passed them twice through sterile PBS and once with medium. For the scarce human tumors, we did these washes in sterile tubes instead.

For human cuboids, MC38 mouse cuboids, and Py8119 cuboids (cytokine, checkpoint inhibitor, and drug panel experiments), the culture medium was Williams' Media E (Sigma) supplemented with nicotinamide (12 mM), L- ascorbic acid 2-phosphate (50 mg/mL), D-(+)-glucose (5 mg/mL) from Sigma; sodium bicarbonate (2.5%), HEPES (20 mM), sodium pyruvate (1 mM), Glutamax (1%), and penicillin–streptomycin (0.4%) from Gibco; and ITS + Premix (1%) and human EGF (20 ng/mL) from BD Biosciences. For other Py8119 experiments (*e.g.*, immunostaining, RPPA, and proteomics), cuboid culture medium was DMEM/F12 with 5% heat-inactivated FBS and 0.1% penicillin-streptomycin. We prepared 80% collagen (Corning rat tail collagen type 1, 354236, 3-4 mg/mL) with 10% 10x PBS, and 10% serum-free medium. We then used filtered-sterilized 1M NaOH to neutralize the pH to ~7.2.

The details for cuboid handling for individual patients were as follows. For patient 1, we performed 2D immunostaining and viability measures as well as pseudo-H&E of a needle biopsy. Slices were cultured overnight after the biopsy and made into cuboids (considered as day 0). Cuboids were grown in 1 mL of collagen on a Transwell insert (PICMORG50, Millipore) in 6-well plates with an air liquid interface and analyzed for viability and drug response using RealTime-Glo (Promega), followed by immunostaining. For patient 2, we performed pseudo-H&E on day 0 cuboids. For patient 3, we cultured cuboids in a 96 well plate, followed by 3D immunostaining and imaging in the microfluidic device. For patient 4, we performed 3D immunostaining on cuboids cultured in microwell devices, followed by immunostaining and imaging in the device. Day 0 controls were immediately fixed, immunostained in microfuge tubes, and imaged in a custom slide. For patient 5, cuboids were either grown in a 6-well plate for multi-IHC, or on the following day, placed individually into a 384-well plate for drug treatment using a custom pipetting robot[39] using medium plus 1% bovine serum albumin (BSA) (Sigma, Rockland). For patient 6, cuboids cut

from patient slices were cultured in a 6-well plate for multi-IHC or manually pipetted into a U bottom 96-well plate at 1 or 8 cuboids per well for drug treatment.

Drug Treatment and Functional Assays

To measure viability, RealTime-Glo (RTG) (Promega) was added at 1x or 0.5x and after overnight incubation, the baseline luminescence was read by IVIS (PerkinElmer). Drug was added to the well, and luminescence was read again after incubation with drug without further addition of RTG. Low viability for patient cuboids (individual or wells) was defined as less than 33% RTG luminescence of the mean (excluding the high outliers), except for in collagen (<10% of mean). To measure cell death as an endpoint, SYTOX Green (1/50,000; Invitrogen) or propidium iodide (1 µg/mL), and/or Hoechst (16 µM, Invitrogen) were added to the well, incubated 1 hr at 37 °C, then imaged with or without washing twice in PBS. For drug panel experiments, multiple cuboids were randomly distributed by manual pipetting, and baseline viability was used to remove outliers before randomly assigning treatments. Cytokine measurements on supernatant were performed by Luminex (Py8119) or by nELISA (CRC-LM, Nomic Bio).

Cuboids were treated with lipopolysaccharide (Sigma L4516) or drugs. Antibodies to checkpoint inhibitors (10 µg/mL) were mouse anti-human PD-1 antibody (BD Biosciences, 562138, clone EH12.1), mouse IgG1 control (BD Biosciences 554721), rat anti-mouse PD-1 antibody (Leinco Technologies, P372), and rat IgG2a control (Leinco Technologies, R1367). Drugs for treatment of cuboids included cisplatin (MedChemExpress), staurosporine (Thermo Scientific), and fluorouracil, oxaliplatin, irinotecan, and cobimetinib (Selleck).

The 35 drug panel for treatment of Py8119 cuboids, in order, was DMSO, Baricitinib (LY3009104, INCB028050), Doramapimod, JNK Inhibitor VIII, TCS ERK 11e (ERK Inhibitor VIII, VX-11e), Rho Kinase Inhibitor III Rockout, PP121, GZD824, Staurosporine, AZD3463, NVP-BVU972, Y-39983 dihydrochloride, cobimetinib, WZ3146, Aminopurvalanol A, SB202190 (FHPI), PD 166285 dihydrochloride, BIIB-057 (PRT062607, P505-15), Akt Inhibitor VIII Isozyme Selective Akti-1/2, CP 547,632, Bosutinib, AT7867, Cdk1/2 Inhibitor III, PDK1/Akt/Flt Dual Pathway Inhibitor, SB 218078, PF-3644022, LY 333531 mesylate (Ruboxistaurin), Cot inhibitor-2, PD 173955 Analogue 1, Vargatef (Nintedanib), BIBF 1120), K252a, Nilotinib, GSK650, Regorafenib, Pazopanib, and At9283. Drugs were obtained from MedChemExpress, Selleck Chemicals, TOCRIS, Cayman, or Sigma.

Microfluidic Device Fabrication and Use

Microchannels were made in a process adapted from Horowitz et al.[37] We designed the devices in AutoCAD (Autodesk), and then fabricated them by laser micromachining (VLS3.60, Scottsdale, USA) of PMMA substrates followed by thermal solvent bonding and adhesive bonding. The device has four layers. The 800 µm-thick PMMA channel network layer (Clarex, Astra Products) has laser-cut microchannels that connect the outflow channel(s) to microtraps via binaries. The microtraps were approximately 560 µm in diameter at the top and 620 µm at the bottom. The microchannels were approximately 410 µm wide except for near the traps where they were approximately 320 µm wide. After sonication of the microchannel layer in isopropanol for 1 min, we bonded it to a 300 µm-thick PMMA sealing layer (Clarex, Astra Products) using thermal solvent bonding; we

exposed both layers to chloroform vapor (~3 mm above the liquid) for 4 min, manually pressed them together, then sealed in a heat press for 5 min at 140 °C, 240-260 psi. The well plate layer was laser-cut from 6.35 mm-thick PMMA (1227T569, McMaster-Carr, Elmhurst, IL) and bonded to the channel layer using double-sided 3M™ High-Strength Acrylic Adhesive 300LSE for 2 min at 250 psi in the thermal press. Silicone tubing was bonded to the outlets using cyanoacrylate glue. Optionally, an additional well plate layer was hand-bonded onto the device after cuboid loading using the 300 LSE. The devices were sterilized by running 70% ethanol through the channels.

To load cuboids into the devices, cuboids were suspended in ice-cold 20% polyethylene glycol (8k-PEG P2139, Sigma-Aldrich) and pipetted into the well. Suction was applied with a 60-cc syringe and a syringe pump (Chemyx Inc.) at 200 mL/hr for 96-microtrap wells or 100 mL/hr for 48-microtrap wells. Mouse cuboids were pushed around the well slowly using either a custom window (single-well, 96-trap device), or a comb (3-well device). For the scarce human cuboids, under visualization with a VHX-970F microscope (Keyence), cuboids were pushed manually to the vicinity of the traps using forceps to encourage only one cuboid per trap. More PEG solution and more cuboids were loaded as needed. The loading process took about 10 min for the 96-trap wells and 1 min for each 48-trap well. The device was placed into a 10 cm petri dish for culture.

Immunostaining and Histology

For multi-immunohistochemistry experiments, tissue pieces and cuboids were fixed in 4% paraformaldehyde and washed with PBS. Cuboids were then embedded in Histogel (Epredia) plugs. Tissue was then processed for microarrays, paraffin sectioning, hematoxylin & eosin (H&E) staining, and multi-immunohistochemistry (multi-IHC) by the Experimental Histopathology Service at the Fred Hutchinson Cancer Research Center. Paraffin section (4 µm) were stained using the Leica BOND Rx stainer and processed with either two 5-plex (mouse) or three 3-plex (human) stains. Lists of antibodies are given in **Table S1**. Staining for tumor cells (CK19) was weak and variable so was not used for quantitation. DAPI was used as a nuclear counterstain.

For peroxidase immunostaining (**Fig. S1**), tissue was fixed in 4% paraformaldehyde overnight then cryoprotected with 30% sucrose/PBS overnight two times. Cryosections (14 µm thickness) were then processed for H&E or for immunostaining. For immunostaining, we pretreated with 0.6% hydrogen peroxide in methanol for 30 min, washed, and then performed antigen retrieval by steaming for 30 min in 10 mM sodium citrate, 0.05% Tween 20 (Sigma), pH 6.0. After at least 30-min block in blocking solution (Tris-NaCl-blocking buffer or TNB buffer, Perkin Elmer, with 0.1% Triton X-100), we incubated the tissues with rabbit primary antibodies (diluted in TNB) overnight at 4 °C. Antibodies were: active cleaved caspase 3 (1/600, Cell Signaling), Ki-67 (1/1,000, AbCAM, ab15580), CD31 (1/200, AbCAM ab28364), or CD45 (1/1,000, AbCAM, ab10558). After incubation of the tissues with an anti-rabbit peroxidase polymer (Vector Labs MP7401) for 30 min, we visualized the staining with 3,3'-Diaminobenzidine (DAB, Vector Labs) and a light hematoxylin counterstain. Washes between steps were done with PBS except for just before DAB incubation, done with 10 mM Tris pH 7.5.

We performed whole-mount immunostaining in the microfluidic devices with a protocol adapted from Li et al.[79] Cuboids were incubated in block (PBS + 0.3% Triton + 1% BSA + 1% normal mouse serum) for >12 hrs at 37 °C on a shaker, then in primary antibody diluted in block for 2 days at 37 °C on a shaker. Primary antibodies were Alexa 647 anti-mouse CD45 (1:200; Biolegend), Alexa 488 anti-mouse CD31 (1:250; Biolegend), Alexa 647 anti-human CD45 (1:400; HI30 Biolegend 304056), rabbit anti-human/mouse cleaved-caspase 3 (1:300; Cell Signaling, 9661), followed by 1:500 546-Donkey/Goat anti-rabbit (or other). We then washed the cuboids 3 times with PBS at least 8 hrs total at 37 °C on a shaker. For the unlabeled primary we incubated with Alexa 546 donkey anti-rabbit IgG (1:500; Invitrogen) diluted in block for 2 days at 37 °C on a shaker followed by washing as above. DAPI 1 µg/mL was added to the last antibody step. We then cleared the tissue by incubation in previously prepared Ce3D solution overnight at room temperature with shaking. The day 0 human ICC cuboids were immunostained in a centrifuge tube and imaged in a custom well.

Whole-mount pseudo-H&E staining (TO-PRO-3 and eosin, ethyl cinnamate clearing) and open-top light-sheet microscopy of a needle biopsy and cuboids (embedded in low-melt agarose) were performed by Alpenglow Biosciences, Inc., with methods described previously.[37]

Imaging and Image Analysis

We took images using a Canon DS126601 on a Nikon SMZ1000 dissecting scope, a Nikon Eclipse Ti microscope, a BZ-X800 (Keyence) microscope, or a Leica SP8 confocal microscope (10x, 2 µm Z steps, at the Lynn & Mike Garvey Imaging Core at the University of Washington). For confocal imaging of 3D immunostaining, we only imaged cuboids at the bottom of a well. For general image manipulation we used FIJI. For patient tumors, we noticed correlations for certain optical features of tumor regions. Some regions looked lighter with top-illumination, dark with through-illumination, and brighter with green autofluorescence. Also visible were regions with blood that were red with top-illumination, dark with through-illumination, and very dark with green autofluorescence. We used FIJI to estimate cuboid size and for measurements of mean fluorescence. We defined regions of interest using a binary mask and removed clumps of cuboids from analysis (in bulk culture). For RTG luminescence, we defined wells as regions of interest using a black and white photograph taken in parallel.

Multi-IHC imaging utilized the Vectra Polaris Quantitative Pathology Imaging System (Akoya Biosciences, Marlborough, MA). Images were spectrally unmixed using Phenoptics inForm software and exported as multi-image TIF files. For multi-IHC image analysis, we used HALO and HALO Link (Indica Labs). For cellular analyses, cells were identified by nuclear DAPI stain, then cytoplasmic boundaries were drawn. For antibodies with clear staining, we applied the same settings to all tissues with similar staining, applying minor adjustments as required to staining groups with varied overall signal (Ki-67, CD45, CD3, CD8, and F4/80). For CD3+ determination, we included all cells with CD8 or CD3 staining as CD8 could occlude CD3. For NKp46 staining, which had few cells in cuboids in days 1 through 7 with high background, we performed an automated count for the initial tumor and did a manual count for the cuboids. For area analyses (CD31), we applied the same

settings to all tissues of that tumor type. We used the background staining from CK19 or from NKp46 to determine the total tissue area.

For 3D image analysis, we used Imaris (Oxford Instruments) through the Lynn & Mike Garvey Imaging Core. Cuboid volume was determined by creating a surface with the DAPI channel or background from another channel. CD31 and CD45 surfaces were created using Labkit for machine learning. For CD31, we applied a gaussian blur before further analysis. We trained the classifiers for days 0 and 2 separately on a stack of two cuboids initially, then applied the classifier to all the cuboids in that day's group. For CD45 on mouse, we trained the classifier on day 0, then applied those settings to all the cuboids.

RPPA

Protein microarrays were printed and processed as previously described.[80] Briefly, cuboid lysates (duplicates of 10 cuboids/sample) from the PY8119 syngeneic mouse breast adenocarcinoma cell line were prepared in 2% SDS lysis buffer (stock recipe, pH = 6.8: Tris·HCl 50 mM, 2% SDS, 5% glycerol, EDTA 5 mM, and NaF 1 mM). Immediately before use, we added protease inhibitors and phosphatase inhibitors (β-GP 10mM, PMSF 1 mM, Na_3VO_4 1 mM, and DTT 1 mM) and then printed onto RPPA slides, each containing 16 nitrocellulose pads (Grace Biolabs, GBL505116), using Aushon 2470 microarrayer (Aushon BioSystems). Samples were printed in duplicate and stored at −20 °C until processing. Slides were then washed with 1 M Tris·HCl (pH 9.0) for 2 to 3 days to remove SDS and PBS solution for 10 to 15 min, centrifuged with Thermo Sorvall Legend XTR Refrigerated Centrifuge (Thermo Scientific), and scanned with InnoScan 910 AL (Innopsys) to ensure no residual SDS. Slides were washed with PBS solution 2 to 3 times for 5 min each and then blocked with Odyssey blocking buffer (OBB) (Licor, 927–40000) for 1 hr at room temperature. Afterwards, slides were fitted to hybridization chamber cassettes (Gel Company, AHF16), incubated with primary antibodies on a shaker overnight at 4 °C. The following day, slides were washed with PBS thrice for 10 min each, blocked again with Odyssey blocking buffer (OBB) (Licor, 927–40000), and incubated with IRDye-labeled secondary antibodies for 1 hr at room temperature. After incubation, slides were washed in PBS 3 times for 10 min each, centrifuged again with Thermo Sorvall Legend XTR Refrigerated Centrifuge (Thermo Scientific), and scanned using Licor Odyssey CLx Scanner (LiCOR). Total signal intensity was normalized to total beta-actin (Sigma, Catalogue No A1978) and quantified using Array-Pro analyzer software package (Media Cybernetics, Maryland, USA). To enable the generation of the heatmap and Pearson correlation figures, we replaced 0 values with the lowest detected values from the other treatments.

Cuboid Sample Preparation for Mass Spectrometry Analysis

Four PBS-washed cuboids per replicate were resuspended in 40 µL of lysis buffer (6M GuHCL, 50 mM Tris pH 8.2, 75 mM NaCl, 10 mM TCEP, 30 mM CAA). The cuboid suspension was subjected to 4 rounds of agitation at 90°C for 5 min followed by 15 min of bath sonication at 40°C. Alkylation was quenched with 15 mM DTT for 30 min at room temperature and the samples were diluted 5-fold with Tris 50 mM pH 8.9 prior to digestion, which was carried out overnight at 37°C using LysC at a 5 ng/µL concentration.

Digestion was quenched with 1% TFA prior to desalting with oasis prime HLB µElution (Waters). Desalted peptides were dried down by vacuum centrifugation.

Mass Spectrometry Data Acquisition

Lyophilized peptide samples were resuspended in 3% ACN, 5% formic acid and subjected to liquid chromatography coupled to tandem mass spectrometry (LC-MS/MS). Samples were loaded into a 100 µm ID x 3 cm precolumn packed with Reprosil C18 1.9 µm, 120 Å particles (Dr. Maisch). Peptides were eluted over a 100 µm inner diam. (I.D.) x 30 cm analytical column packed with the same material housed in a column heater set to 50 °C and separated by gradient elution of 6 to 38% B (A: 0.15% FA , B: ACN 80% and 0.15% FA) over 65 min and 38% to 50% B over 8 min at 400 nL/min delivered by an Easy1200 nLC system (Thermo Fisher Scientific) with a total 90 min method length. Peptides were online analyzed on an Orbitrap Eclipse Tribrid mass spectrometer (Thermo Fisher Scientific). Mass spectra were collected using a data-independent acquisition method. For each cycle a full MS scan (358-1100 m/z, resolution 60,000, and Standard 100% normalized AGC target in automatic maximum injection time mode) followed by 30 consecutive non-overlapping MS/MS scans with 24 m/z wide isolation windows. MS/MS scans were acquired at 30,000 resolution in centroid mode, using HCD fragmentation with 33% normalized collision energy and an 800% normalized AGC target with automatic maximum injection time mode. In alternating cycles, the mass target list for MS/MS scans was offset by 12 m/z to produce DIA windows with half overlap spanning the 363-1095 m/z mass range. Information on Mass spectrometry Data Analysis is supplied in Suppl. Info. The mass spectrometry proteomics data was deposited to the ProteomeXchange Consortium via the PRIDE partner repository (https://www.ebi.ac.uk/pride/).

Statistical analysis

Graphpad Prism 7 was used for statistics unless otherwise noted. Post-hoc power analysis (80% power and α=0.05) was performed using https://clincalc.com/stats/samplesize.aspx.

References

1. Letai, A. Functional precision cancer medicine—moving beyond pure genomics. *Nat. Med.* **23**: 1028–1035 (2017).
2. Wu, K. Z., Adine, C., Mitriashkin, A., Aw, B. J. J., Iyer, N. G. & Fong, E. L. S. Making In Vitro Tumor Models Whole Again. *Adv. Healthc. Mater.* **12**: 2202279 (2023).
3. Hutchinson, L. & Kirk, R. High drug attrition rates—where are we going wrong? *Nat. Rev. Clin. Oncol.* **8**: 189 (2011).
4. Ocana, A., Pandiella, A., Siu, L. L. & Tannock, I. F. Preclinical development of molecular-targeted agents for cancer. *Nat. Rev. Clin. Oncol.* **8**: 200–209 (2010).
5. Ghaemmaghami, A. M., Hancock, M. J., Harrington, H., Kaji, H. & Khademhosseini, A. Biomimetic tissues on a chip for drug discovery. *Drug Discov. Today* **17**: 173–181 (2012).
6. Jin, M. Z., Han, R. R., Qiu, G. Z., Ju, X. C., Lou, G. & Jin, W. L. Organoids: An intermediate modeling platform in precision oncology. *Cancer Lett.* **414**: 174–180 (2018).
7. Sontheimer-Phelps, A., Hassell, B. A. & Ingber, D. E. Modelling cancer in microfluidic human organs-on-chips. *Nat. Rev. Cancer* **19**: 65–81 (2019).

8. Gray, H. J. *et al.* Extraordinary clinical response to ibrutinib in low-grade ovarian cancer guided by organoid drug testing. *npj Precis. Oncol.* **7**: 45 (2023).
9. Nguyen, H. T. *et al.* Engineered Vasculature for Cancer Research and Regenerative Medicine. *Micromachines* **14**: 978 (2023).
10. LeSavage, B. L., Suhar, R. A., Broguiere, N., Lutolf, M. P. & Heilshorn, S. C. Next-generation cancer organoids. *Nat. Mater.* **21**: 143–159 (2022).
11. Dougan, M., Dranoff, G. & Dougan, S. K. Cancer Immunotherapy: Beyond Checkpoint Blockade. *Annu. Rev. Cancer Biol.* **3**: 55–75 (2019).
12. Kruger, S., Ilmer, M., Kobold, S., Cadilha, B. L., Endres, S., Ormanns, S., Schuebbe, G., Renz, B. W., D'Haese, J. G., Schloesser, H., Heinemann, V., Subklewe, M., Boeck, S., Werner, J. & von Bergwelt-Baildon, M. Advances in cancer immunotherapy 2019 – latest trends. *J. Exp. Clin. Cancer Res.* **38**: 268 (2019).
13. Murciano-Goroff, Y. R., Warner, A. B. & Wolchok, J. D. The future of cancer immunotherapy: microenvironment-targeting combinations. *Cell Res.* **30**: 507–519 (2020).
14. Xin Yu, J., Hodge, J. P., Oliva, C., Neftelinov, S. T., Hubbard-Lucey, V. M. & Tang, J. Trends in clinical development for PD-1/PD-L1 inhibitors. *Nat. Rev. Drug Discov.* **19**: 163–164 (2020).
15. Meijer, T. G., Naipal, K. A., Jager, A. & van Gent, D. C. Ex vivo tumor culture systems for functional drug testing and therapy response prediction. *Futur. Sci. OA* **3**: FSO190 (2017).
16. Astolfi, M., Peant, B., Lateef, M. A., Rousset, N., Kendall-Dupont, J., Carmona, E., Monet, F., Saad, F., Provencher, D., Mes-Masson, A. M. & Gervais, T. Micro-dissected tumor tissues on chip: an ex vivo method for drug testing and personalized therapy. *Lab Chip* **16**: 312–325 (2016).
17. Dorrigiv, D., Simeone, K., Communal, L., Kendall-Dupont, J., St-Georges-robillard, A., Péant, B., Carmona, E., Mes-Masson, A. M. & Gervais, T. Microdissected tissue vs tissue slices—a comparative study of tumor explant models cultured on-chip and off-chip. *Cancers (Basel).* **13**: 4208 (2021).
18. Horowitz, L. F., Rodriguez, A. D., Dereli, Z., Lin, R., Mikheev, A. M., Monnat Raymond J., J., Folch, A. & Rostomily, R. C. Multiplexed drug testing of tumor slices using a microfluidic platform. *Nat. Precis. Oncol.* **4**: 12 (2020).
19. Rodriguez, A., Horowitz, L. F., Castro, K., Yeung, R. S., Rostomily, R. C. & Folch, A. A microfluidic platform for the delivery of panels of drugs to live tumor slices. *Lab Chip* **20**: 1658–1675 (2020).
20. Moore, N., Doty, D., Zielstorff, M., Kariv, I., Moy, L. Y., Gimbel, A., Chevillet, J. R., Lowry, N., Santos, J., Mott, V., Kratchman, L., Lau, T., Addona, G., Chen, H. & Borenstein, J. T. A multiplexed microfluidic system for evaluation of dynamics of immune-tumor interactions. *Lab Chip* **18**: 1844–1858 (2018).
21. Aref, A. R. *et al.* 3D microfluidic ex vivo culture of organotypic tumor spheroids to model immune checkpoint blockade. *Lab Chip* **18**: 3129–3143 (2018).
22. Sivakumar, R., Chan, M., Shin, J. S., Nishida-Aoki, N., Kenerson, H. L., Elemento, O., Beltran, H., Yeung, R. & Gujral, T. S. Organotypic tumor slice cultures provide a versatile platform for immuno-oncology and drug discovery. *Oncoimmunology* **8**: e1670019 (2019).
23. Vaira, V., Fedele, G., Pyne, S., Fasoli, E., Zadra, G., Bailey, D., Snyder, E., Faversani, A., Coggi, G., Flavin, R., Bosari, S. & Loda, M. Preclinical model of organotypic culture for pharmacodynamic profiling of human tumors. *Proc. Natl. Acad. Sci.* **107**: 8352–8356 (2010).
24. Jagatia, R., Doornebal, E. J., Rastovic, U., Harris, N., Feyide, M., Lyons, A. M., Miquel, R.,

Zen, Y., Zamalloa, A., Malik, F., Prachalias, A., Menon, K., Boulter, L., Eaton, S., Heaton, N., Phillips, S., Chokshi, S. & Palma, E. Patient-derived precision cut tissue slices from primary liver cancer as a potential platform for preclinical drug testing. *eBioMedicine* **97**: 104826 (2023).

25. Powley, I. R., Patel, M., Miles, G., Pringle, H., Howells, L., Thomas, A., Kettleborough, C., Bryans, J., Hammonds, T., MacFarlane, M. & Pritchard, C. Patient-derived explants (PDEs) as a powerful preclinical platform for anti-cancer drug and biomarker discovery. *Br. J. Cancer* **122**: 735–744 (2020).
26. Ricciardelli, C., Lokman, N. A., Sabit, I., Gunasegaran, K., Bonner, W. M., Pyragius, C. E., Macpherson, A. M. & Oehler, M. K. Novel ex vivo ovarian cancer tissue explant assay for prediction of chemosensitivity and response to novel therapeutics. *Cancer Lett.* **421**: 51–58 (2018).
27. Polak, R., Zhang, E. T. & Kuo, C. J. Cancer organoids 2.0: modelling the complexity of the tumour immune microenvironment. *Nat. Rev. Cancer* **24**: 523–539 (2024).
28. Voabil, P., de Bruijn, M., Roelofsen, L. M., Hendriks, S. H., Brokamp, S., van den Braber, M., Broeks, A., Sanders, J., Herzig, P., Zippelius, A., Blank, C. U., Hartemink, K. J., Monkhorst, K., Haanen, J. B. A. G., Schumacher, T. N. & Thommen, D. S. An ex vivo tumor fragment platform to dissect response to PD-1 blockade in cancer. *Nat. Med.* **27**: 1250–1261 (2021).
29. Majumder, B. *et al.* Predicting clinical response to anticancer drugs using an ex vivo platform that captures tumour heterogeneity. *Nat. Commun.* **6**: 6169 (2015).
30. Jenkins, R. W. *et al.* Ex vivo profiling of PD-1 blockade using organotypic tumor spheroids. *Cancer Discov.* **8**: 196–215 (2018).
31. LeBlanc, V. G., Trinh, D. L., Aslanpour, S., Hughes, M., Livingstone, D., Jin, D., Ahn, B. Y., Blough, M. D., Cairncross, J. G., Chan, J. A., Kelly, J. J. P. & Marra, M. A. Single-cell landscapes of primary glioblastomas and matched explants and cell lines show variable retention of inter- and intratumor heterogeneity. *Cancer Cell* **40**: 379-392.e9 (2022).
32. Neal, J. T. *et al.* Organoid Modeling of the Tumor Immune Microenvironment. *Cell* **175**: 1972-1988.e16 (2018).
33. Li, X. *et al.* Oncogenic transformation of diverse gastrointestinal tissues in primary organoid culture. *Nat. Med.* **20**: 769–777 (2014).
34. Cordts, S. C., Yuki, K., Henao Echeverri, M. F., Narasimhan, B., Kuo, C. J. & Tang, S. K. Y. Microdissection tools to generate organoids for modeling the tumor immune microenvironment. *Microsystems Nanoeng.* **10**: 126 (2024).
35. Chatzidimitriou, F. A Platform to Restore Intra-Tissue Flow in Live Explant Assays. *Ph.D. thesis, Imperial College London (Bioengineering Department)* (2021) doi:https://doi.org/10.25560/100935.
36. Crosby, D., Bhatia, S., Brindle, K. M., Coussens, L. M., Dive, C., Emberton, M., Esener, S., Fitzgerald, R. C., Gambhir, S. S., Kuhn, P., Rebbeck, T. R. & Balasubramanian, S. Early detection of cancer. *Science* **375**: 1244 (2022).
37. Horowitz, L. F., Rodriguez, A. D., Au-Yeung, A., Bishop, K. W., Barner, L. A., Mishra, G., Raman, A., Delgado, P., Liu, J. T. C., Gujral, T. S., Mehrabi, M., Yang, M., Pierce, R. H. & Folch, A. Microdissected “cuboids” for microfluidic drug testing of intact tissues. *Lab Chip* **21**: 122 (2021).
38. Lockhart, E. J., Horowitz, L. F., Rodriguez, A., Zhu, S., Nguyen, T., Mehrabi, M., Gujral, T. S. & Folch, A. Drug testing of monodisperse arrays of live microdissected tumors using a valved multiwell microfluidic platform. *Lab Chip* **24**: 2683 (2024).

39. Stepanov, I., Gottshall, N. R., Ahmadianyazdi, A., Sinha, D., Lockhart, E. J., Nguyen, T. N. H., Hassan, S., Horowitz, L. F., Yeung, R., Gujral, T. S. & Folch, A. Low-Cost Robotic Manipulation of Live Microtissues for Cancer Drug Testing. *BioRxiv* https://doi.org/10.1101/2024.03.21.586169 (2024).
40. Nguyen, T. N. H., Horowitz, L., Krilov, T., Lockhart, E., Kenerson, H. L., Gujral, T. S., Yeung, R. S., Arroyo-Currás, N. & Folch, A. Label-Free, Real-Time Monitoring of Cytochrome C Drug Responses in Microdissected Tumor Biopsies with a Multi-Well Aptasensor Platform. *Sci. Adv.* **10**: eadn5875 (2024).
41. Groebe, K. & Mueller-Klieser, W. On the relation between size of necrosis and diameter of tumor spheroids. *Int. J. Radiat. Oncol.* **34**: 395–401 (1996).
42. Singh, M., Venkata Krishnan, H., Ranganathan, S., Kiesel, B., Beumer, J. H., Sreekumar, S. & Sant, S. Controlled Three-Dimensional Tumor Microenvironments Recapitulate Phenotypic Features and Differential Drug Response in Early vs Advanced Stage Breast Cancer. *ACS Biomater. Sci. Eng.* **4**: 421–431 (2018).
43. Zheng, Y., Chen, J., Craven, M., Choi, N. W., Totorica, S., Diaz-Santana, A., Kermani, P., Hempstead, B., Fischbach-Teschl, C., López, J. a & Stroock, A. D. In vitro microvessels for the study of angiogenesis and thrombosis. *Proc. Natl. Acad. Sci. U. S. A.* **109**: 9342–7 (2012).
44. Aguilera, T. A., Rafat, M., Castellini, L., Shehade, H., Kariolis, M. S., Hui, A. B. Y., Stehr, H., Von Eyben, R., Jiang, D., Ellies, L. G., Koong, A. C., Diehn, M., Rankin, E. B., Graves, E. E. & Giaccia, A. J. Reprogramming the immunological microenvironment through radiation and targeting Axl. *Nat. Commun.* **7**: 13898 (2016).
45. Lu, C., Liu, Y., Ali, N. M., Zhang, B. & Cui, X. The role of innate immune cells in the tumor microenvironment and research progress in anti-tumor therapy. *Front. Immunol.* **13**: 1039260 (2023).
46. Sathe, A., Mason, K., Grimes, S. M., Zhou, Z., Lau, B. T., Bai, X., Su, A., Tan, X., Lee, H. J., Suarez, C. J., Nguyen, Q., Poultsides, G., Zhang, N. R. & Ji, H. P. Colorectal Cancer Metastases in the Liver Establish Immunosuppressive Spatial Networking between Tumor-Associated SPP1+ Macrophages and Fibroblasts. *Clin. Cancer Res.* **29**: 244–260 (2023).
47. Ozga, A. J., Chow, M. T. & Luster, A. D. Chemokines and the immune response to cancer. *Immunity* **54**: 859–874 (2021).
48. Jenkins, R. W. *et al.* Ex vivo profiling of PD-1 blockade using organotypic tumor spheroids. *Cancer Discov.* **8**: 196–215 (2018).
49. Bhat, A. A., Nisar, S., Singh, M., Ashraf, B., Masoodi, T., Prasad, C. P., Sharma, A., Maacha, S., Karedath, T., Hashem, S., Yasin, S. B., Bagga, P., Reddy, R., Frennaux, M. P., Uddin, S., Dhawan, P., Haris, M. & Macha, M. A. Cytokine- and chemokine-induced inflammatory colorectal tumor microenvironment: Emerging avenue for targeted therapy. *Cancer Commun.* **42**: 689–715 (2022).
50. Bazzichetto, C., Milella, M., Zampiva, I., Simionato, F., Amoreo, C. A., Buglioni, S., Pacelli, C., Le Pera, L., Colombo, T., Bria, E., Zeuli, M., Del Bufalo, D., Sperduti, I. & Conciatori, F. Interleukin-8 in Colorectal Cancer: A Systematic Review and Meta-Analysis of Its Potential Role as a Prognostic Biomarker. *Biomedicines* **10**: 2631 (2022).
51. Binnewies, M. *et al.* Targeting TREM2 on tumor-associated macrophages enhances immunotherapy. *Cell Rep.* **37**: 109844 (2021).
52. Jin, Y., An, X., Mao, B., Sun, R., Kumari, R., Chen, X., Shan, Y., Zang, M., Xu, L., Muntel, J., Beeler, K., Bruderer, R., Reiter, L., Guo, S., Zhou, D., Li, Q. X. & Ouyang, X. Different syngeneic tumors show distinctive intrinsic tumor-immunity and mechanisms of actions

(MOA) of anti-PD-1 treatment. *Sci. Rep.* **12**: 3278 (2022).
53. Morris, V. K. *et al.* Treatment of Metastatic Colorectal Cancer: ASCO Guideline. *J. Clin. Oncol.* **41**: 678–700 (2023).
54. Rodriguez, H., Zenklusen, J. C., Staudt, L. M., Doroshow, J. H. & Lowy, D. R. The next horizon in precision oncology: Proteogenomics to inform cancer diagnosis and treatment. *Cell* **184**: 1661–1670 (2021).
55. Martínez-Val, A., Fort, K., Koenig, C., Van der Hoeven, L., Franciosa, G., Moehring, T., Ishihama, Y., Chen, Y. ju, Makarov, A., Xuan, Y. & Olsen, J. V. Hybrid-DIA: intelligent data acquisition integrates targeted and discovery proteomics to analyze phospho-signaling in single spheroids. *Nat. Commun.* **14**: 3599 (2023).
56. Myers, S. A., Rhoads, A., Cocco, A. R., Peckner, R., Haber, A. L., Schweitzer, L. D., Krug, K., Mani, D. R., Clauser, K. R., Rozenblatt-Rosen, O., Hacohen, N., Regev, A. & Carr, S. A. Streamlined protocol for deep proteomic profiling of FAC-sorted cells and its application to freshly isolated murine immune cells. *Mol. Cell. Proteomics* **18**: 995–1009 (2019).
57. Satpathy, S. *et al.* Microscaled proteogenomic methods for precision oncology. *Nat. Commun.* **11**: 532 (2020).
58. Armstrong, H. K., Gillis, J. L., Johnson, I. R. D., Nassar, Z. D., Moldovan, M., Levrier, C., Sadowski, M. C., Chin, M. Y., Tomlinson Guns, E. S., Tarulli, G., Lynn, D. J., Brooks, D. A., Selth, L. A., Centenera, M. M. & Butler, L. M. Dysregulated fibronectin trafficking by Hsp90 inhibition restricts prostate cancer cell invasion. *Sci. Rep.* **8**: 2090 (2018).
59. van Maldegem, F., Valand, K., Cole, M., Patel, H., Angelova, M., Rana, S., Colliver, E., Enfield, K., Bah, N., Kelly, G., Tsang, V. S. K., Mugarza, E., Moore, C., Hobson, P., Levi, D., Molina-Arcas, M., Swanton, C. & Downward, J. Characterisation of tumour microenvironment remodelling following oncogene inhibition in preclinical studies with imaging mass cytometry. *Nat. Commun.* **12**: 5906 (2021).
60. Saraon, P., Pathmanathan, S., Snider, J., Lyakisheva, A., Wong, V. & Stagljar, I. Receptor tyrosine kinases and cancer: oncogenic mechanisms and therapeutic approaches. *Oncogene* **40**: 4079–4093 (2021).
61. Hsu, Y. H. *et al.* Definition of PKC-α, CDK6, and MET as therapeutic targets in triple-negative breast cancer. *Cancer Res.* **74**: 4822–4835 (2014).
62. Kaboli, P. J., Chen, H.-F., Babaeizad, A., Geraylow, K. R., Yamaguchi, H. & Hung, M.-C. Unlocking c-MET: A comprehensive journey into targeted therapies for breast cancer. *Cancer Lett.* **588**: 216780 (2024).
63. van de Wetering, M. *et al.* Prospective Derivation of a Living Organoid Biobank of Colorectal Cancer Patients. *Cell* **161**: 933–945 (2015).
64. Sachs, N. *et al.* A Living Biobank of Breast Cancer Organoids Captures Disease Heterogeneity. *Cell* **172**: 373-386.e10 (2018).
65. Kopper, O. *et al.* An organoid platform for ovarian cancer captures intra- and interpatient heterogeneity. *Nat. Med.* **25**: 838–849 (2019).
66. Zhang, Y., Zhen-Yu, W., Hong-Shu, J., Hong-Dan, Z., He-Xin, Y., Jian-Xia, F. & Zhai, B. A pre-clinical model combining cryopreservation technique with precision-cut slice culture method to assess the in vitro drug response of hepatocellular carcinoma. *Int. J. Mol. Med.* **49**: 51 (2022).
67. Bazou, D., Maimon, N., Gruionu, G., Grahovac, J., Seano, G., Liu, H., Evans, C. L. & Munn, L. L. Vascular beds maintain pancreatic tumour explants for ex vivo drug screening. *J. Tissue Eng. Regen. Med.* **12**: e318–e322 (2018).
68. Hubert, C. G., Rivera, M., Spangler, L. C., Wu, Q., Mack, S. C., Prager, B. C., Couce, M.,

McLendon, R. E., Sloan, A. E. & Rich, J. N. A three-dimensional organoid culture system derived from human glioblastomas recapitulates the hypoxic gradients and cancer stem cell heterogeneity of tumors found in vivo. *Cancer Res.* **76**: 2465–2477 (2016).
69. Fang, Z., Li, P., Du, F., Shang, L. & Li, L. The role of organoids in cancer research. *Exp. Hematol. Oncol. 2023 121* **12**: 1–21 (2023).
70. Marusyk, A., Janiszewska, M. & Polyak, K. Intratumor Heterogeneity: The Rosetta Stone of Therapy Resistance. *Cancer Cell* **37**: 471–484 (2020).
71. Li, J., Van Vranken, J. G., Pontano Vaites, L., Schweppe, D. K., Huttlin, E. L., Etienne, C., Nandhikonda, P., Viner, R., Robitaille, A. M., Thompson, A. H., Kuhn, K., Pike, I., Bomgarden, R. D., Rogers, J. C., Gygi, S. P. & Paulo, J. A. TMTpro reagents: a set of isobaric labeling mass tags enables simultaneous proteome-wide measurements across 16 samples. *Nat. Methods* **17**: 399 (2020).
72. Edwards, N. J., Oberti, M., Thangudu, R. R., Cai, S., McGarvey, P. B., Jacob, S., Madhavan, S. & Ketchum, K. A. The CPTAC data portal: A resource for cancer proteomics research. *J. Proteome Res.* **14**: 2707–2713 (2015).
73. Whiteaker, J. R. *et al.* CPTAC Assay Portal: a repository of targeted proteomic assays. *Nat. Methods* **11**: 703–704 (2014).
74. van Bentum, M. & Selbach, M. An Introduction to Advanced Targeted Acquisition Methods. *Mol. Cell. Proteomics* **20**: 100165 (2021).
75. Stopfer, L. E., Flower, C. T., Gajadhar, A. S., Patel, B., Gallien, S., Lopez-Ferrer, D. & White, F. M. High-Density, Targeted Monitoring of Tyrosine Phosphorylation Reveals Activated Signaling Networks in Human Tumors. *Cancer Res.* **81**: 2495 (2021).
76. Summers, H. D., Wills, J. W. & Rees, P. Spatial statistics is a comprehensive tool for quantifying cell neighbor relationships and biological processes via tissue image analysis. *Cell Reports Methods* **2**: 100348 (2022).
77. Carr, S. A. *et al.* Targeted peptide measurements in biology and medicine: Best practices for mass spectrometry-based assay development using a fit-for-purpose approach. *Mol. Cell. Proteomics* **13**: 907–917 (2014).
78. Ryu, H. *et al.* Transparent, Compliant 3D Mesostructures for Precise Evaluation of Mechanical Characteristics of Organoids. *Adv. Mater.* **33**: 2100026 (2021).
79. Li, W., Germain, R. N. & Gerner, M. Y. High-dimensional cell-level analysis of tissues with Ce3D multiplex volume imaging. *Nat. Protoc.* **14**: 1708–1733 (2019).
80. Gujral, T. S., Karp, R. L., Finski, A., Chan, M., Schwartz, P. E., Macbeath, G. & Sorger, P. Profiling phospho-signaling networks in breast cancer using reverse-phase protein arrays. *Oncogene* **32**: 3470–3476 (2013).

Acknowledgments

We thank Heidi Kenerson for preparation of human slices. This research was supported by the Experimental Histopathology Shared Resource of the Fred Hutch/University of Washington Cancer Consortium (P30 CA015704).

Funding: NCI grants R21CA251952 (AF, TSG), 2R01 CA181445 (AF, TSG), R01 CA272677 (AF, RY, TSG), NIGMS grant R35GM119536, NHGRI grant RM1HG010461 (RR, JV), and UW Bridge Funding (JV).

Author contributions:

Conceptualize: LFH, RR, JV, TSG, AF
Methodology: LFH, RR, JV, TSG, AF
Performed experiments: LFH, RR, SZ, NRG, IS, MY, TNHN, EJL, TSG
Supervision: RSY, JV, TSG, AF
Visualization and analysis: LFH, RR, SZ, CS, MY
Writing: LFH, RR, JV, TSG, AF

Competing interests: L.F.H. and A.F. are the founders of OncoFluidics, a startup that seeks to commercialize drug tests using intact tissues and microfluidic technology. L.H and A.F. are inventors in U.S. patent No. US 9,518,977 (filed 13 Dec 2016) and US patent applications No. 63/428,542 (filed 29 Nov 2022) and No. 18/652334 (filed 1 May 2024) related to this work.

Data and materials availability: Multi-IHC and 3D imaging data and analysis are available on reasonable request. The mass spectrometry proteomics data have been deposited to the ProteomeXchange Consortium via the PRIDE partner repository (https://www.ebi.ac.uk/pride/). All other data are available in the main text or in the supplementary materials.

Figures

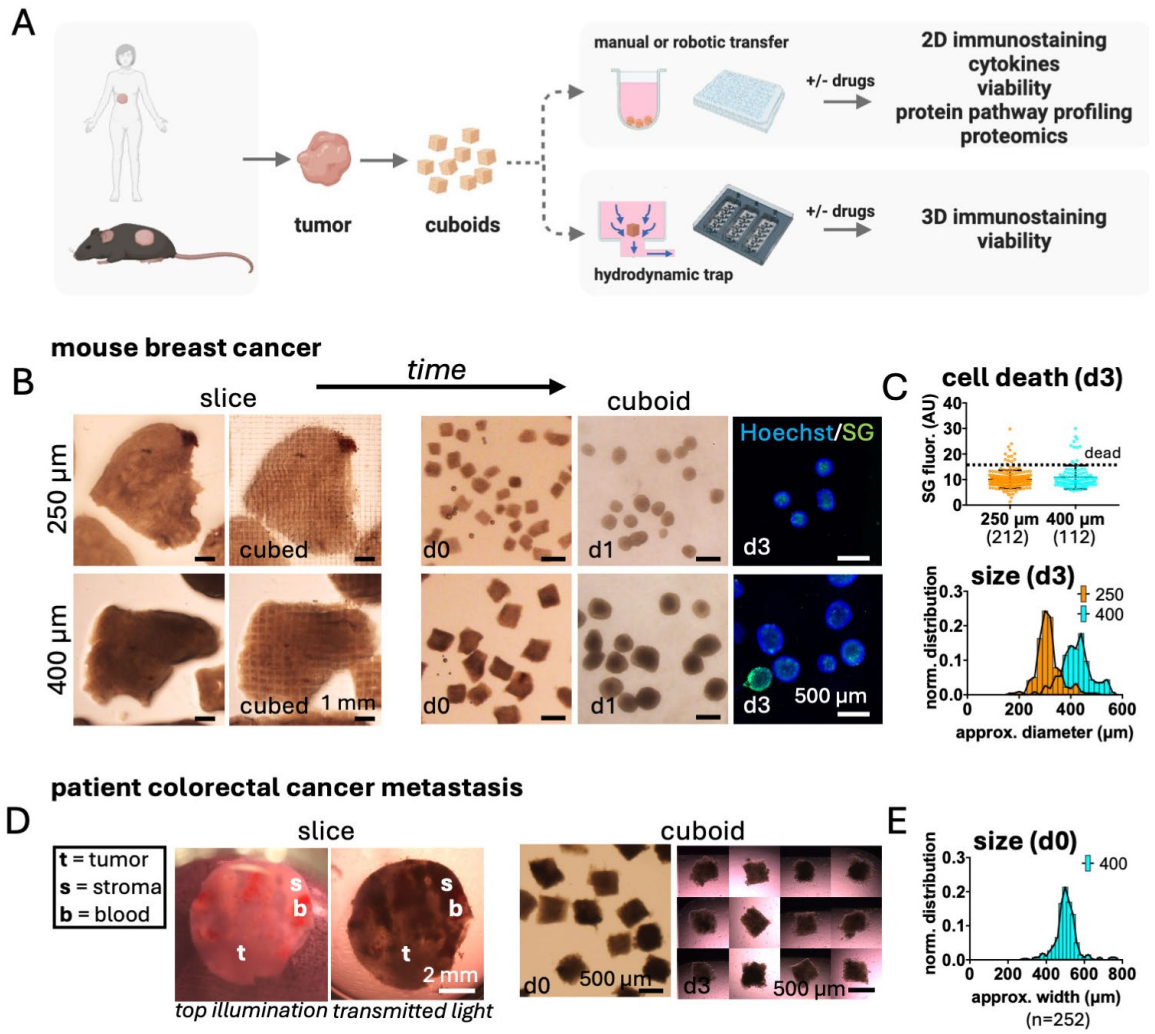

Fig. 1. Cuboid generation and culture. (**A**) Schematic of cuboid workflow. (**B**) Sequential formation and culture of 250- µm or 400-µm mouse Py8119 breast cancer syngeneic tumor cuboids, with vibratome sectioning to make slices, tissue chopper to make polygonal cuboids at day 0 (d0), and spherical morphology at day 1 (d1) and day 3 (d3). Viability was assessed at day 3 using the SYTOX Green dye (SG) for dead nuclei and the Hoechst blue dye for all nuclei. Cuboids were cultured in 6-well plates. (C) Graphs of viability (ave ± SD; dashed line for viability cutoff) and size (histogram) of mouse cuboids at d3. (**D**) Human colorectal cancer liver metastasis (CRC-LM) slice visualized with either top illumination or through illumination (bottom), cuboids at d0 and at d3 (in a 384-well plate). (**E**) Size histogram of cuboid sizes at d0.

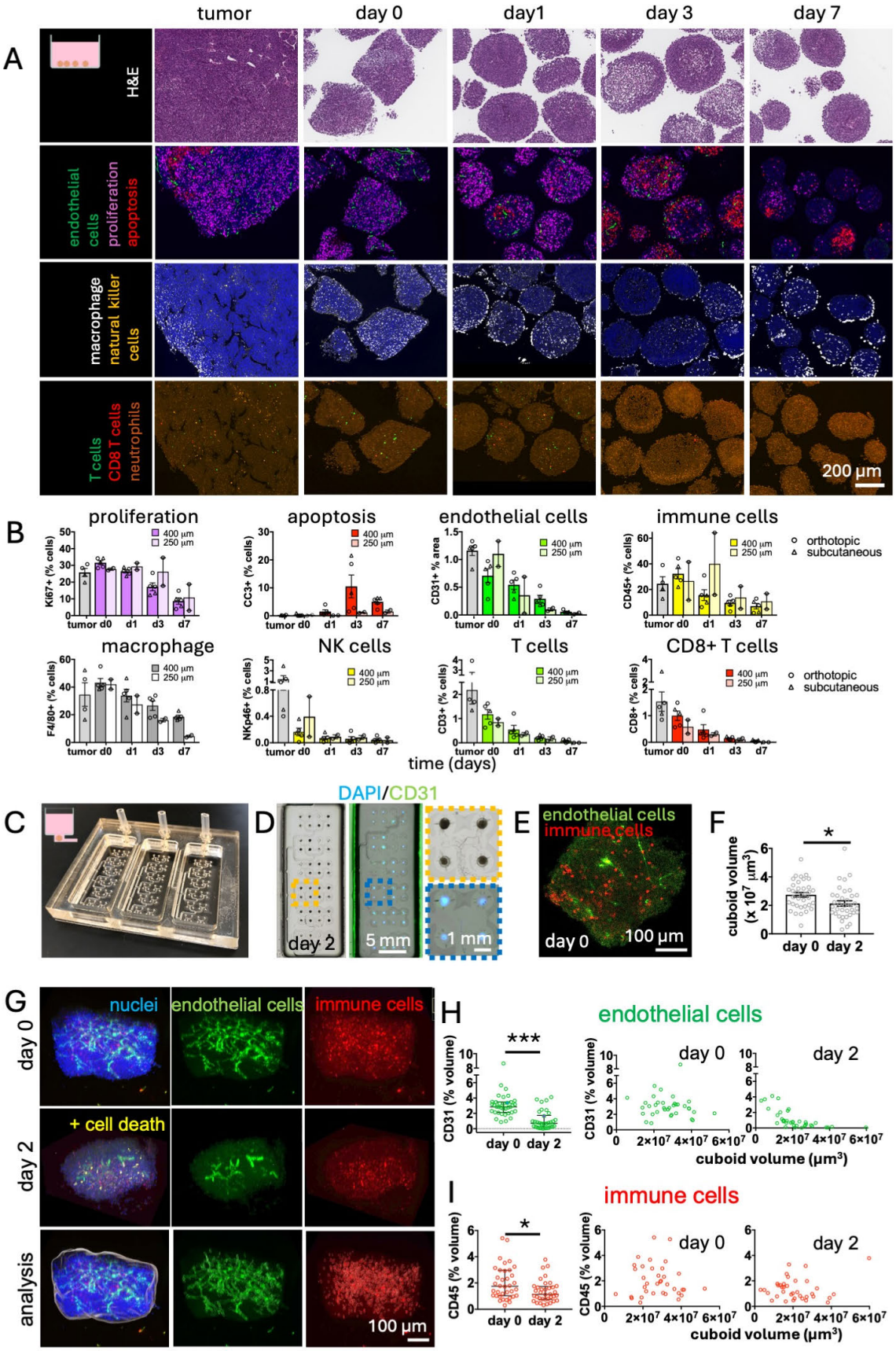

Fig. 2. Characterization of the mouse cuboid and its TME. (**A,B**) Histology and fluorescent multi-immunohistochemistry (multi-IHC) of mouse Py8119 breast cancer cuboids grown in a 6-well plate. (**A**) Representative images of histology (H&E) and multi-IHC of 400-µm

cuboids (from orthotopic tumor shown), including apoptotic cell death (cleaved-caspase 3, CC3), proliferation (Ki67), and multiple cell types. (**B**) Quantitation of multi-IHC staining of 400-µm cuboids (n=5 and ave ± sem) and 250-µm cuboids (n=2, ave and range). Individual points represent the mean value for that time point for the total surface area encompassing multiple cuboids (11-40 for 400-µm cuboids) for each tumor. 2 subcutaneous tumors (∆) and 3 orthotopic tumors (o). (**C-H**) Whole-mount immunostaining of orthotopic Py8119 mouse cuboids at day 0 and day 2. (**C**) Microfluidic device used for on-device immunostaining, clearing, and confocal imaging. 3 independent wells each have 48 cuboid traps each connected by binaries to 1 output. (**D**) One well showing Py8119 mouse cuboids in the device after 2 days in culture and immunostaining (CD31 for endothelial cells, CD45 for immune cells, cleaved-caspase-3 for cell death, DAPI nuclear stain), and clearing with Ce3D. (**E**) Confocal image of immunostaining for day 0. (**F**) Graph of cuboid volume. Ave ± sem. n=34-36 cuboids. Student's T-test, *p<0.05. (**G**) 3D images of cuboids stained in the traps with example of Imaris 3D analysis for day 0. (**H,I**) Graphs showing quantitation of endothelial and immune cell staining versus volume for individual cuboids (points). Median and quartile. n=34-36 cuboids. Mann-Whitney test. *p<0.05, ***p<0.0001. Endothelial cells (CD31), immune cells (CD45), macrophage (F4/80), NK cells (NKp46), T cells (CD3), cytotoxic T cells (CD8), and neutrophils (Ly6G).

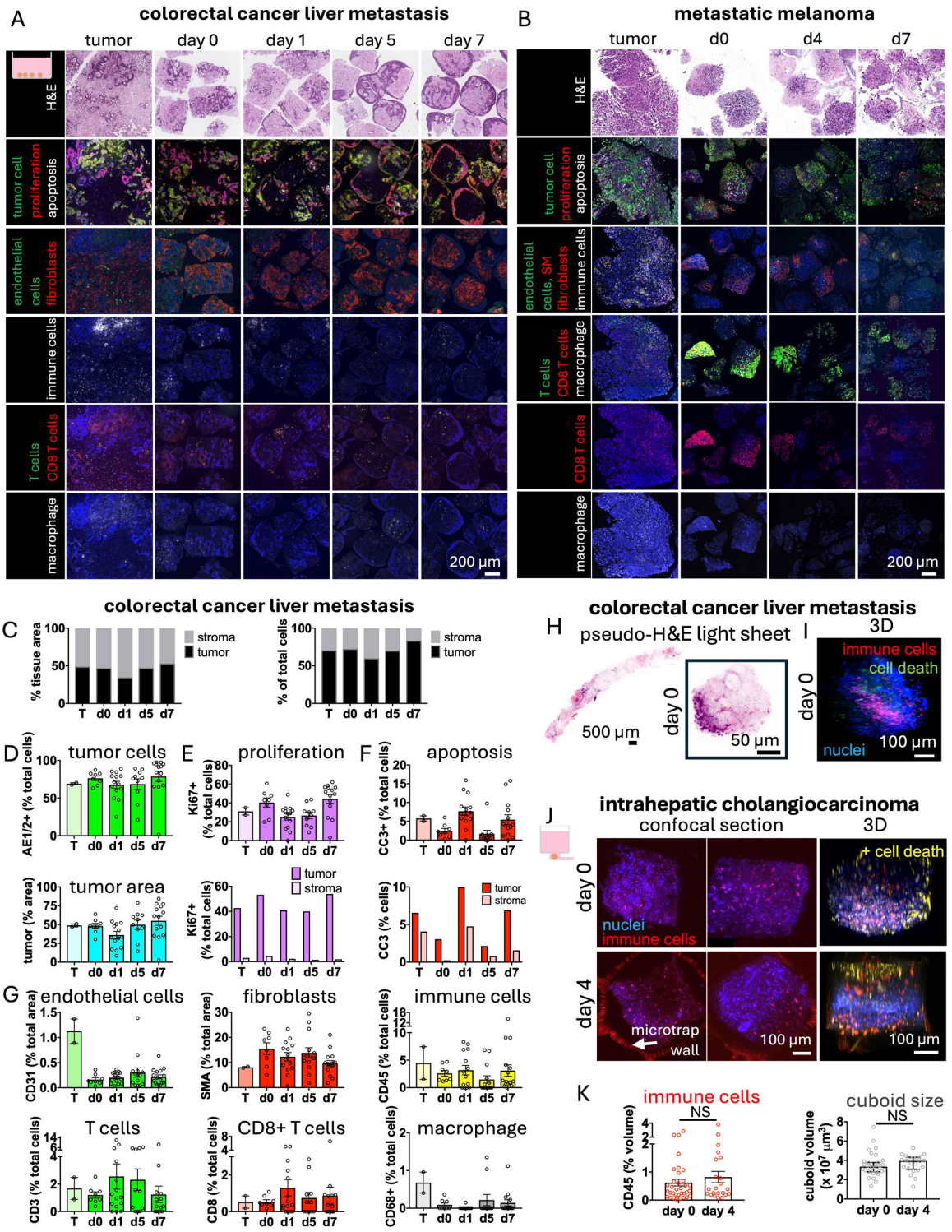

Fig. 3. Characterization of heterogeneous patient cancer cuboids and their TME. (**A,B**) Histology and multi-IHC of a colorectal cancer liver metastasis (CRC-LM) (**A**) and a patient metastatic melanoma lymph node (**B**). 400-µm cuboids were cultured in 6-well plates and sampled from day 1 (d1) to day 7 (d7), as well as before culturing (d0) and in the initial tumor (T). DAPI nuclear stain in blue. Cell type antibodies: tumor cells (colon cancer: AE1/AE2; melanoma: Mel mix), endothelial cells (CD31), fibroblasts and smooth muscle cells (smooth muscle actin), immune cells (CD45), macrophage (human: CD68), T cells (CD3), and cytotoxic T cells (CD8). (**C-G**) Quantitation of staining in (**A**) using HALO, with

breakdown of staining into “tumor” and “stromal” subregions in (**C-F**). (**H**) Pseudo-H&E optical section using open top light sheet microscopy of a needle biopsy and cuboid (inset) from a CRC-LM. (**I**) Confocal 3D rendering of a CRC-LM cuboid immunostained with CD45 for immune cells, cleaved-caspase-3 for cell death, and a DAPI nuclear stain. (**J**) 2D confocal section and 3D renderings of cuboids from a patient idiopathic cholangiocarcinoma at day 0, or after 4 days culture in the microfluidic device. (**K**) Quantitation of immune cells (% of total cuboid volume) and of cuboid volume, n=34 (day 0) and n=22 (day 4) cuboids. Ave ± sem. Student’s T-test, NS.

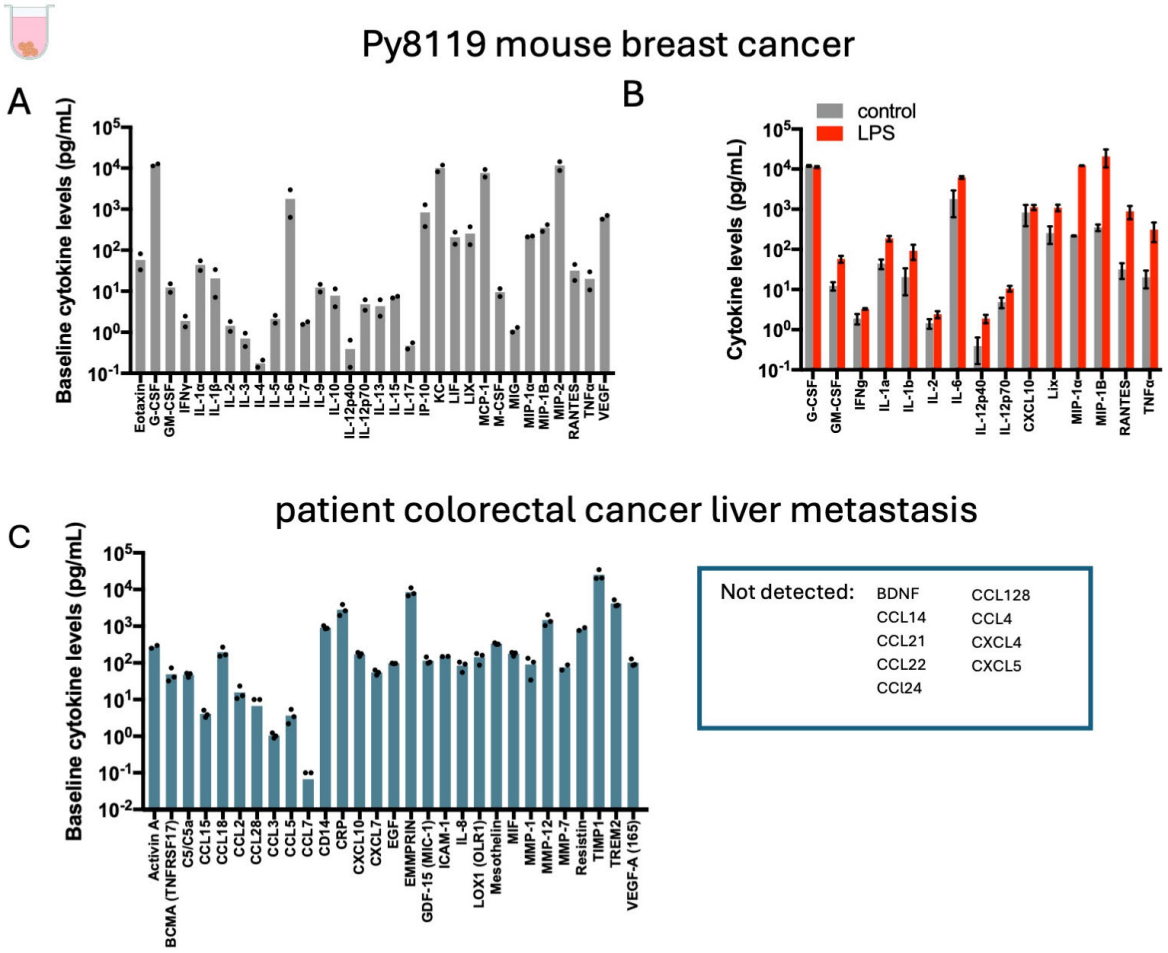

Fig. 4. Cuboid cytokine secretion. Cytokine/chemokine secretion in 400-µm cuboids grown in 96 well plates. (**A**) Baseline cytokine secretion from Py8119 mouse breast cancer cuboids by Luminex. 2-6 cuboids/well. Individual replicates shown. (**B**) Cytokine response in Py8119 mouse breast cancer cuboids after 24 hour exposure to LPS (lipopolysaccharide, 1 µg/mL) to activate the innate immune system in comparison to control (**A**) (subset of cytokines shown). (**C**) Baseline secretion of cytokines and other factors from human colorectal cancer liver metastasis (CRC-LM) cuboids. 29 positive signals plus select negative signals of 192 tested by nELISA. 4-6 cuboids per well, day 5.

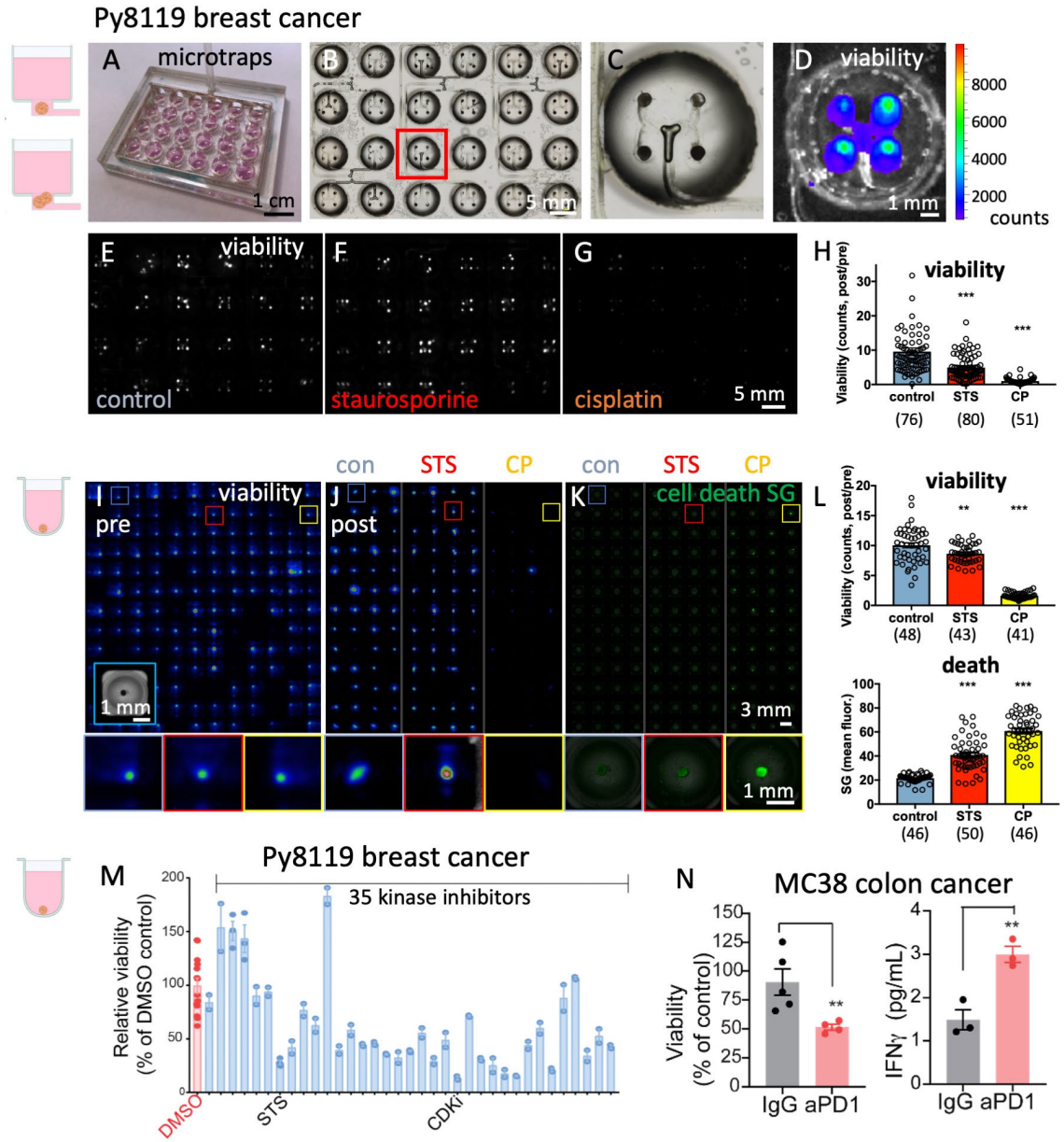

Fig. 5. Drug treatment of mouse tumor cuboids. 400-µm Py8119 mouse breast cancer cuboids were treated in parallel either on a microfluidic device (**A-H**) or with individual cuboids in a 384-well plate (I-M). (**A**) Microfluidic device with 24 wells, 4 traps/well. (**B-D**) Py8119 mouse breast cancer cuboids loaded on a device (**B, C** close-up) with viability by RealTime-Glo (RTG) luminescence imaging (**D**). (**E-G**) Viability after 3 days of drug treatment of 3 different devices with staurosporine (STS, 2 µM) or cisplatin (CP, 100 µM). (**H**) Graph shows changes in viability (post/pre) by luminescence for individual traps (1-3 cuboids each trap). Ave ± sem. Kruskal-Wallis test versus control with Dunns multiple comparisons. ***p<0.001. (I-K) Drug responses of individual cuboids, manually pipetted to have one per well on a 384-well plate, measured for viability by RTG luminescence (**I,J**) and for cell death by SYTOX Green (SG) nuclear stain (**K**). Close-ups shown below. (**L**) Graphs of viability and cell death, with responses of individual cuboids (circles) and ave ± sem. One way ANOVA, Tukey post-hoc. ***p<0.0005. n=41-50. (**M**) Responses of mouse Py8119 cuboids to a panel of 34 kinase inhibitors (1 µM). Viability (post/pre) measured by RTG luminescence before and after 3 day treatment, given as a % of the DMSO control.

Duplicates of 2-6 cuboids/well. Staurosporine (STS) and CDK4/6 (CDKi) kinase inhibitor positive controls. (**N**) Responses of MC38 subcutaneous mouse colon cancer cuboids to checkpoint inhibitor immunotherapy for 4 days with anti-PD-1 versus IgG control, with decreased viability (RTG) and increased IFNγ secretion. 6-12 cuboids per well. Ave ± sem. Student's T-test **p<0.01.

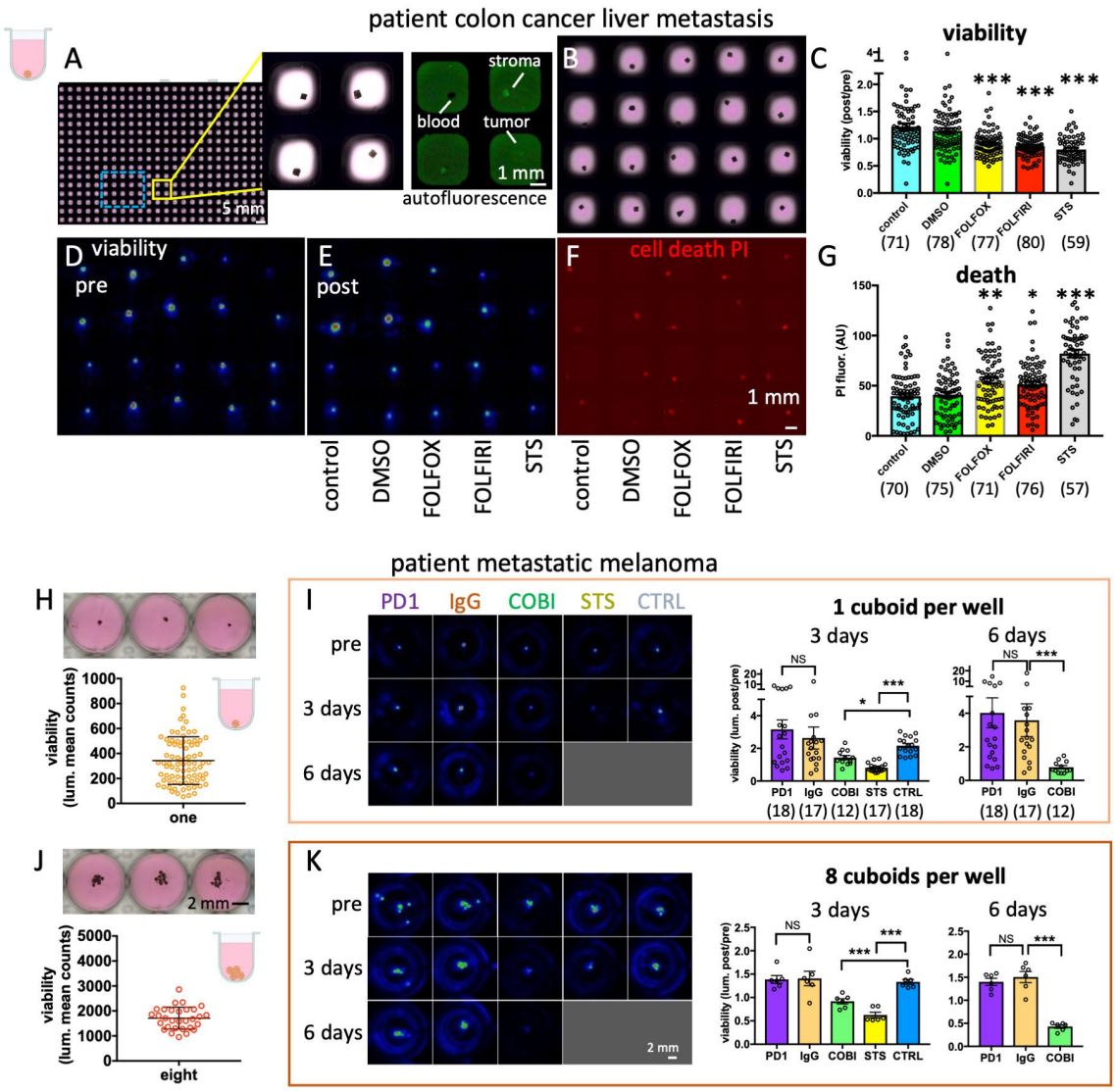

Fig. 6. Drug treatment of human cuboids. (**A-G**) Drug treatment of 400-µm patient colorectal cancer liver metastasis cuboids, transferred by a robot to a 384-well plate (**A**), with 1 cuboid per well and close-ups of yellow region showing heterogeneity revealed by green autofluorescence. After exposure to drugs for 5 days, viability was measured by RealTime-Glo (RTG) luminescence and death was measured by propidium iodide (PI). (**B, D-F**) Close-ups of blue rectangle in (**A**), with pre-treatment RTG viability on day 2 (**D**), and day 7 post treatment RTG viability (**E**) and propidium iodide staining for cell death. (**F**) Graph of viability by RTG with post/pre for each cuboid. (**G**) Graph of cell death by PI. Responses of individual cuboids (circles) and average ± sem. Kruskal-Wallis test with Dunn's multiple comparison. 8 wells with two cuboids per well not included. DMSO (0.2%). FOLFOX (1 µg/mL 5-fluorouracil, 1 µg/mL oxaliplatin). FOLFIRI (1 µg/mL 5-fluorouracil, 2 µg/mL irinotecan), STS (staurosporine 1 µM). Ave ± sem. Kruskal-Wallis test with Dunn's multiple comparisons versus DMSO. *p<0.05. **p<0.01. ***p<0.0005. (**H-K**) Cuboids from a patient metastatic melanoma lymph node biopsy after 6 day treatment with checkpoint inhibitor (PD-1), IgG control, the MEK kinase inhibitor cobimetinib (COBI, 1 µM), staurosporine (STS), or control (CTRL). (**H,J**) Cuboids image and graph of RTG viability for individual wells at day 1 for single (**H**) or for eight (**J**) cuboids per well. (**I,K**) Representative

images of RTG viability and graphs (post/pre) for one (**I**) or for two (**K**) cuboids per well. Number of wells indicated for single cuboid wells, n=6 for eight cuboid wells. Mann-Whitney and Kruskal-Wallis rank order tests. *$p<0.05$. ***$p<0.001$.

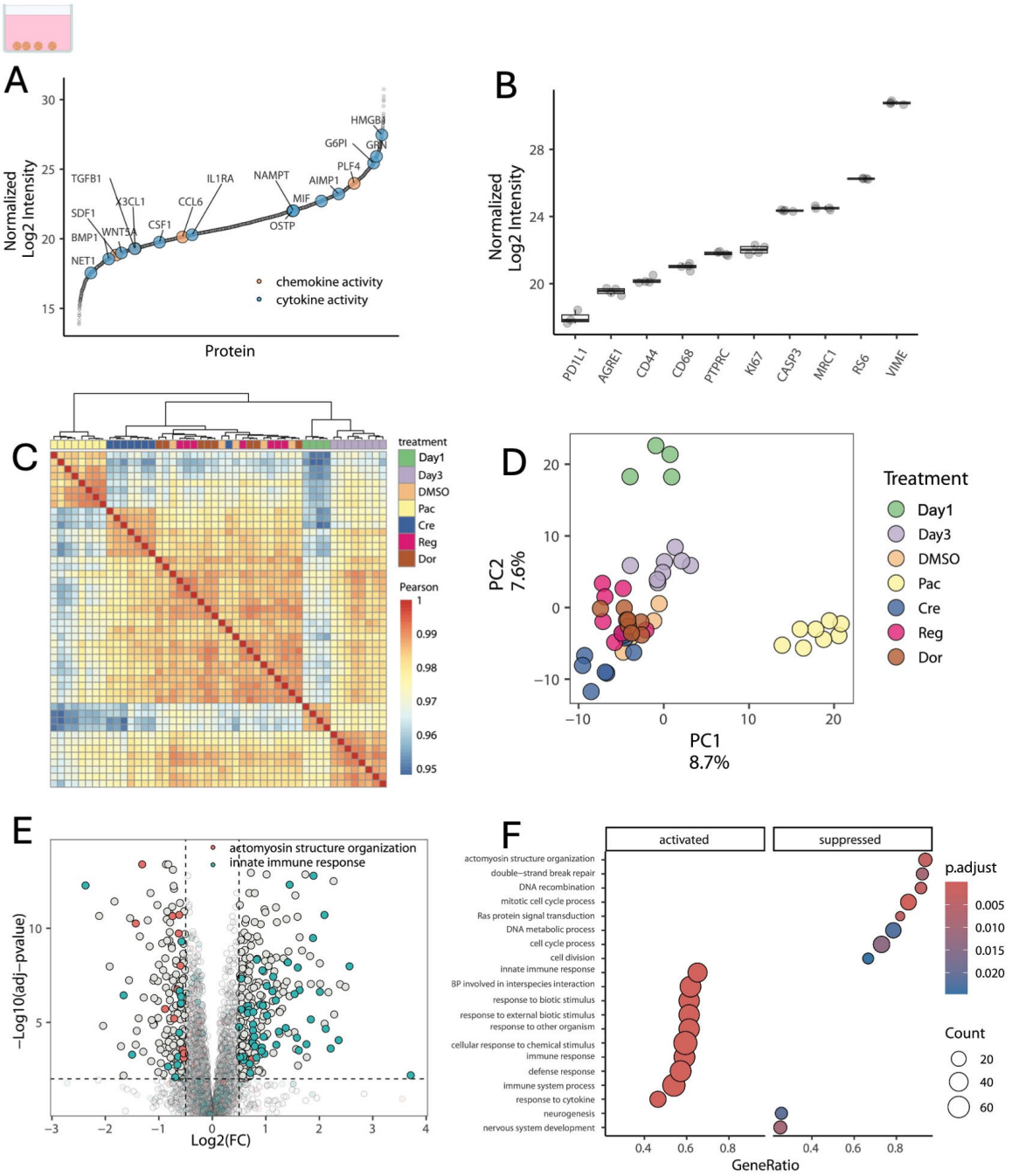

Fig. 7. Profiling the proteomes of mouse breast cancer cuboids using mass spectrometry and their changes upon drug treatments. (**A,B**) Quantification of TME proteins from 400-µm PY8119 breast cancer cuboids cultured in 6-well plates at day 1, with 4 cuboids per sample. (**A**) Ranked plot for median normalized log2 protein intensities in day 1 samples; highlighted proteins associated with GO terms: chemokine (yellow) and cytokine activities (blue). (**B**) Box and Dot plot of day 1 normalized protein log2 intensities for observed TME markers.[59] (**C-F**) Observed changes to the cuboid proteome upon drug treatment from day 0 to day 3. (**C**) Heat map: Pearson correlations for protein abundances across drug treatments and replicates. Day 1, Day3: untreated controls. Treatments (sampled at day 3): **DMSO** (0.1% DMSO), **Pac**: (10 µM paclitaxel), **Cre** (0.5 µM crenolanib), **Reg** (0.5 µM regorafenib), and **Dor** (0.5 µM doramapimod). (**D**) Dot plot: PC1 and PC2 of principal component analysis for protein abundance measurements across treatments and

replicates. (**E**) Volcano plot: protein abundance log2 fold changes between DMSO and Paclitaxel treatments on day 3 and adjusted p-values. Log2 fold changes and multiple hypothesis testing adjusted p-values calculated using MSStats linear model. Highlighted proteins in (**grey**) with fold change threshold |Log2FC| > 0.5 and adjusted p-value<0.01; associated with Gene Ontology terms: (**blue**) innate immune response, (**red**) actomyosin structure organization. (**F**) Gene Ontology enrichment analysis of Biological Process terms for upregulated and downregulated proteins between DMSO and Paclitaxel treatments.

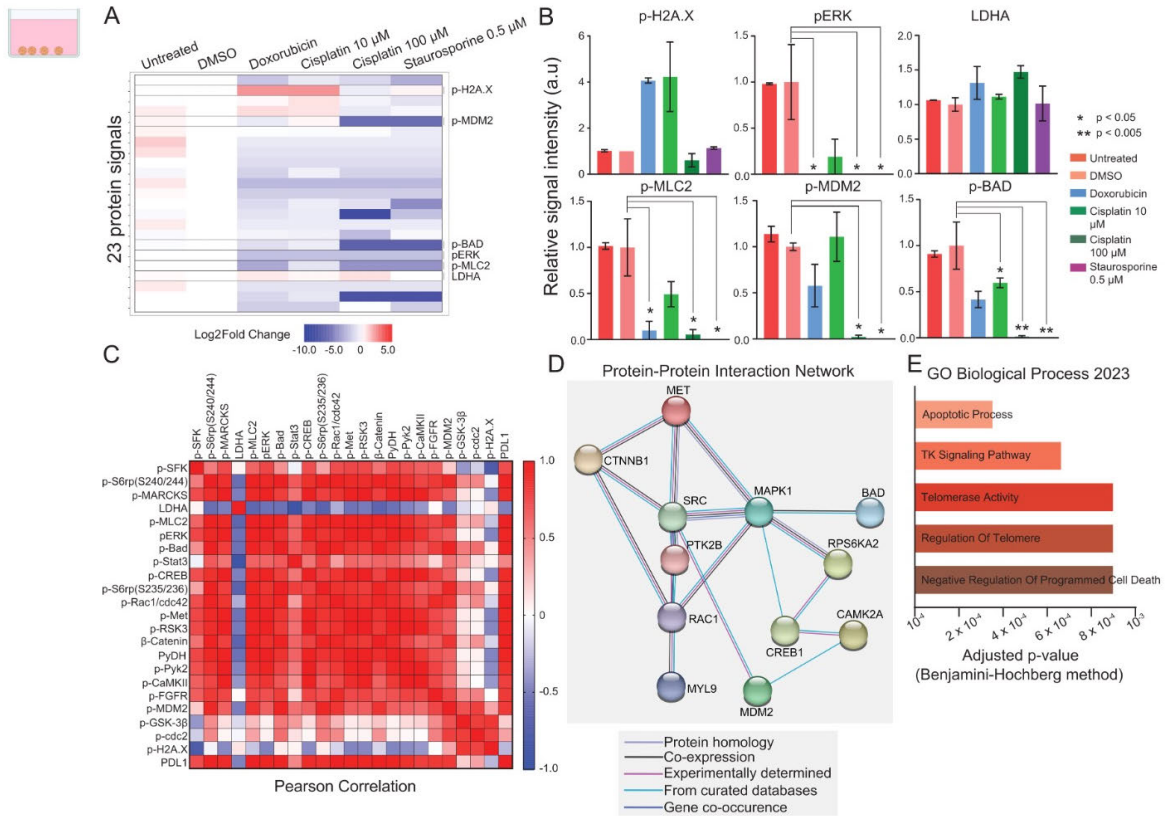

Fig. 8. Profiling changes in signaling pathways from drug-treated 400-µm PY8119 breast cuboids. Reverse-phase protein array (RPPA) was used to profile 48 proteins from PY8119 breast cuboid samples after treatment for 3 days in a 6-well plate (untreated, 0.1% DMSO, Doxorubicin 10 µM, Cisplatin 10 µM, Cisplatin 100 µM, or Staurosporine 2 µM). Data from the 23 high-quality signals are shown. (**A**) Heat map representation of relative signal intensities, normalized in a stepwise manner: beta-actin levels, untreated samples, and DMSO treated samples. (**B**) Graphical representation of relative protein levels from annotated proteins in (**A**), normalized in the same process as in (**A**) except without log2 transformation. Except for p-H2A.X DMSO, n=2 per condition and *p<0.05 unpaired t-tests compared to DMSO. (**C**) Pearson Correlation. The correlation matrix depicts the result of a Pearson correlation analysis performed on the 23 proteins of interest using measurements taken from all samples. (**D**) Protein-protein interaction network from positively correlated proteins in (**C**) (StringDB). (**E**) Gene enrichment analysis using the same positively correlated proteins from (**C**) (Enrichr). Adjusted p-values corrected for multiple hypothesis testing by the Benjamini-Hochberg method. Full names of top biological processes: regulation of apoptotic process, transmembrane receptor protein tyrosine kinase signaling pathway, regulation of telomerase activity, and regulation of telomere maintenance via telomerase.